nature portfolio

https://doi.org/10.1038/s41586-023-06663-8

Supplementary information

Imaging inter-valley coherent order in magic-angle twisted trilayer graphene

Supplementary Information: Imaging inter-valley coherent order in magic-angle twisted trilayer graphene

Hyunjin Kim, Youngjoon Choi, Étienne Lantagne-Hurtubise, Cyprian Lewandowski, Alex Thomson, Lingyuan Kong, Haoxin Zhou, Eli Baum, Yiran Zhang, Ludwig Holleis, Kenji Watanabe, Takashi Taniguchi, Andrea F. Young, Jason Alicea, Stevan Nadj-Perge

Additional data:

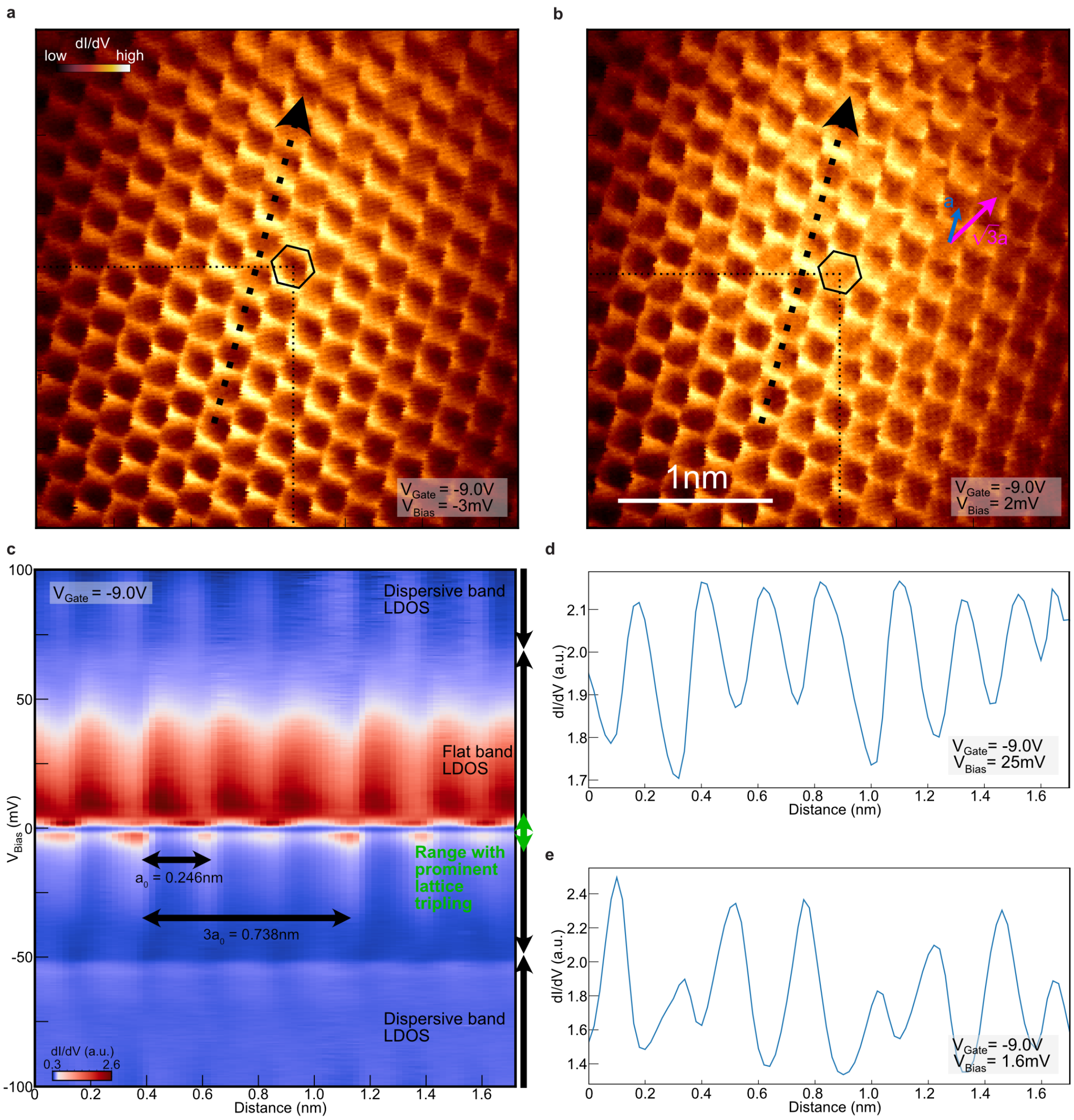

Supplementary Information Fig. 1. **V_{Bias} dependent mapping of the lattice tripling order at $V_{\mathrm{Gate}} = -9$ V. a-b**, 3 nm by 3 nm dI/dV map measured at negative $V_{\mathrm{Bias}} = -3$ mV (**a**) and positive $V_{\mathrm{Bias}} = 2$ mV (**b**). Black dashed arrow shows the spatial position where Fig. 1c is measured and is parallel to one of graphene lattice vectors. Kekulé modulation shows up as $3a_0$ periodicity due to 30° rotation. **c**, Tunneling conductance V_{Bias} linecut taken along spatial points marked by the dashed arrow in **a,b**. While the spatial modulation with the periodicity of a_0 is apparent for all V_{Bias}, modulation with the periodicity of $3a_0$ is only apparent at V_{Bias} near zero as indicated by the green arrows. **d-e**, linecut taken from Fig. 1c at $V_{\mathrm{Bias}} = 25$ mV (**d**) which is around conduction band VHS and a $V_{\mathrm{Bias}} = 1.6$ mV (**e**) which is on the LDOS peak accompanying pseudogap.

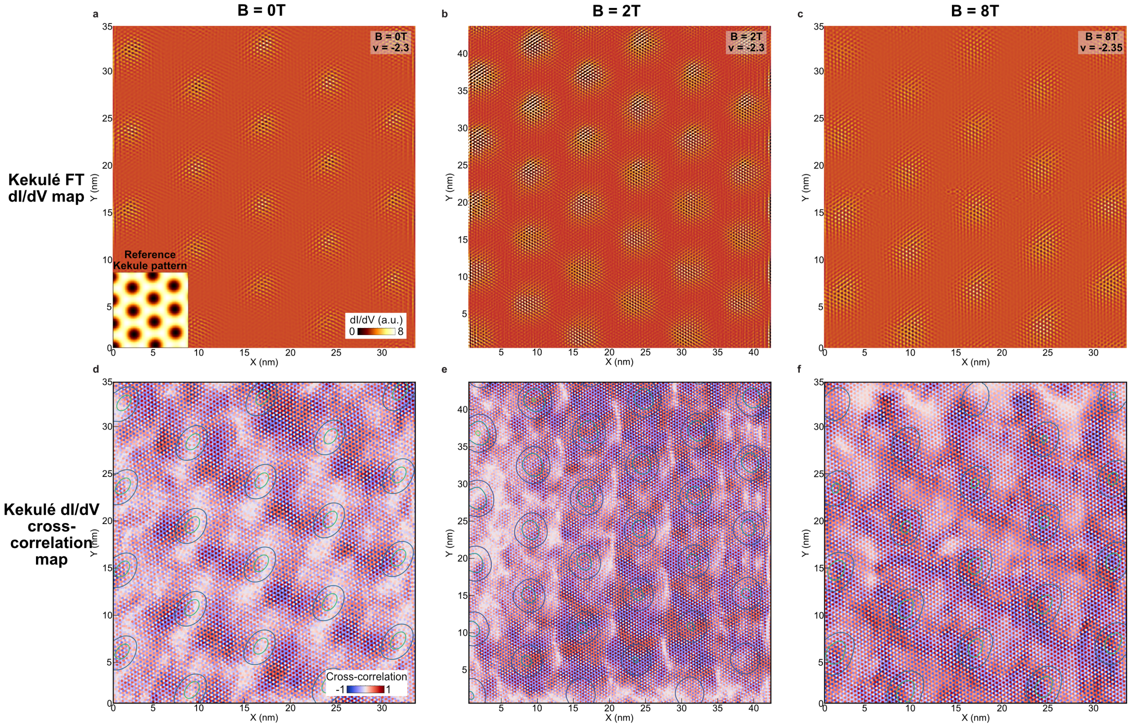

Supplementary Information Fig. 2. **Evolution of Kekulé pattern with out-of-plane magnetic field. a-c**, Kekulé FT filtered dI/dV map taken at $B = 0$ T (**a**), $B = 2$ T (**b**), $B = 8$ T (**c**). V_{Gate} are chosen such that the flat band filling factor correspond to ($\nu = -2.3$). The raw dI/dV map has been used to extract $q_{\mathrm{Kekulé}}$ in main text Fig. 4i. FT filtering is performed by using a round mask of radius 3.5 nm^{-1} around six Kekulé FT peaks. **d-f**, Kekulé dI/dV cross-correlation map of panels a-c. Cross-correlation is calculated between a small window of Kekulé FT dI/dV map and the universal reference Kekulé pattern shown on the inset of **a**. Using this reference plot, we calculated 2D cross-correlation map at different B. The Kekulé patterns evolve rapidly within moiré unit cell for $B = 0$ T and $B = 2$ T. Moreover, this rapid evolution occurs not only in the direction of $q_{\mathrm{Kekulé}}$, but also in the direction perpendicular to it. This is not the case for $B = 8$ T, where more pronounced stripe-like pattern of regions across the neighboring AAA sites are observed. For the highest field the rapid evolution of Kekulé pattern in the direction perpendicular to $q_{\mathrm{Kekulé}}$ is greatly suppressed. A contour plot is an eye-guide showing the centers of AAA sites.

The remainder of this Supplementary Information section provides details of the theoretical modeling supporting this work and is organized as follows. We first establish conventions and review the continuum model for twisted graphene superlattices in Sec. 1, and discuss the influence of a non-zero displacement field induced by a back gate in Sec. 2. We then review the treatment of heterostrain and its profound effects on the low-energy (flat) bands of MATTG in Sec. 3. In Sec. 4, we investigate Hartree corrections to the MATTG flat bands in the presence of strain, focusing on filling factors between -3 and -2. In Sec. 5, we explore various types of inter-valley coherent instabilities in MATTG. In particular, we extract trends related to the preferred IKS wavevector as a function of strain parameters, interaction strength, and the chiral ratio in the BM model.

In Sec. 6 we introduce more formally different inter-valley coherent orders, and in Sec. 7 we present an efficient numerical method to compute real-space lattice tripling signatures in the local density of states (LDOS). We contrast the implications for moiré-periodic IVC orders to those of incommensurate Kekulé spiral (IKS) states in Sec. 8. Finally, in Sec. 9, we speculate on a scenario whereby the incommensurate Kekulé spiral might undergo a lock-in mechanism to a nearby commensurate wavevector.

1. CONVENTIONS, GEOMETRY AND THE BM MODEL

We first establish our conventions. We denote the carbon-carbon length $a_0 = 0.142$ nm. We take the Bravais lattice vectors of monolayer graphene as

$$\boldsymbol{A}_1 = \sqrt{3}a_0 \left(\frac{1}{2}, \frac{\sqrt{3}}{2}\right) \ , \ \boldsymbol{A}_2 = \sqrt{3}a_0 \left(\frac{1}{2}, -\frac{\sqrt{3}}{2}\right) , \tag{1}$$

and its reciprocal lattice vectors

$$\boldsymbol{G}_1 = \frac{4\pi}{3a_0} \left(\frac{\sqrt{3}}{2}, \frac{1}{2}\right) \ , \ \boldsymbol{G}_2 = \frac{4\pi}{3a_0} \left(\frac{\sqrt{3}}{2}, -\frac{1}{2}\right) . \tag{2}$$

The graphene Dirac points are located at $\boldsymbol{K}_\pm = \mp \frac{4\pi}{3\sqrt{3}a_0}(1,0)$. (In the main text, we refer alternatively to the two Dirac points as $\boldsymbol{K}$ and $\boldsymbol{K}'$.)

We consider alternating-twist trilayer graphene (TTG)[1,2] with a twist angle $-\theta/2$ (i.e., in the clockwise direction) applied to the top and bottom layers, and $\theta/2$ (i.e., in the counterclockwise direction) applied to the middle layer. The corresponding moiré pattern is characterized by Bravais lattice vectors

$$\boldsymbol{a}_1 = \frac{4\pi}{3k_\theta} \left(\frac{\sqrt{3}}{2}, \frac{1}{2}\right) \ , \ \boldsymbol{a}_2 = \frac{4\pi}{3k_\theta} (0,1) , \tag{3}$$

and reciprocal lattice vectors

$$\boldsymbol{g}_1 = \sqrt{3}k_\theta (1,0) \ , \ \boldsymbol{g}_2 = \sqrt{3}k_\theta \left(-\frac{1}{2}, \frac{\sqrt{3}}{2}\right) , \tag{4}$$

with $k_\theta = 2|\boldsymbol{K}_\pm| \sin\frac{\theta}{2}$ the momentum scale between the Dirac points originating from (say) the top and middle layers. In the MATTG sample investigated in the main text, the twist angle $\theta = 1.602^\circ$ translates to a moiré lengthscale $l_M = 4\pi/3k_\theta \approx 8.80$ nm.

To describe the low-energy physics of the system our starting point is the continuum Bistritzer-MacDonald (BM) model[3,4], which consists of intra-layer kinetic energy contributions as well as inter-layer tunneling modulated by the moiré potential. We treat the spin degree of freedom as a spectator throughout. In the low-energy (linearized) approximation for the original Dirac cones of each graphene layer, the intra-layer contribution can be written as

$$h^l_\tau(\boldsymbol{k},\theta) = \hbar v_F[R^T(\theta_l)(\gamma_\tau + \boldsymbol{k} - \boldsymbol{K}_{\tau,l})]\cdot(\tau\sigma_x,\sigma_y) \tag{5}$$

where $l = 1,2,3$ denotes the layer and $\tau = \pm$ the valley, σ_x, σ_y are Pauli matrices acting on the sublattice (A/B) degree of freedom, $R(\theta)$ is the usual counter-clockwise rotation matrix and $v_F \sim 8.7 \times 10^5$ m/s is an effective Fermi velocity, similar to the value for monolayer graphene (but larger than the value obtained from fitting to ab initio calculations[5] in TBG).The Dirac point in layer l is rotated as $\boldsymbol{K}_{\tau,l} = R(\theta_l)\boldsymbol{K}_\tau$. The momentum $\gamma_\tau + \boldsymbol{k}$ in Eq. 5 denotes the microscopic momentum of each graphene layer, measured with respect to the original $\boldsymbol{\Gamma}$ point, while $\boldsymbol{k}$ is defined from the mBZ center in each valley, $\gamma_\tau = -\tau\frac{4\pi}{3\sqrt{3}a_0}\left(\sqrt{3}\sin(\frac{\theta}{2}) + \cos(\frac{\theta}{2}), 0\right)$, see Fig. 3a.

The inter-layer tunneling between adjacent graphene layers is modulated by the moiré potential, and reads

$$T(\boldsymbol{r}) = T_1 + T_2 e^{i(\boldsymbol{g}_1+\boldsymbol{g}_2)\cdot\boldsymbol{r}} + T_3 e^{i\boldsymbol{g}_2\cdot\boldsymbol{r}}, \tag{6}$$

where the three matrices

$$T_1 = \begin{pmatrix} w_0 & w_1 \\ w_1 & w_0 \end{pmatrix}, \; T_2 = \begin{pmatrix} w_0 & w_1 e^{-i\phi} \\ w_1 e^{i\phi} & w_0 \end{pmatrix}, \; T_3 = \begin{pmatrix} w_0 & w_1 e^{i\phi} \\ w_1 e^{-i\phi} & w_0 \end{pmatrix}, \tag{7}$$

act in the sublattice space, and the phase factor $\phi = 2\pi/3$. In valley $\tau = -$, the inter-layer tunneling terms are obtained by time-reversal symmetry which (in the spinless version of the problem) flips all momenta and takes $\phi \to -\phi$. For the tunneling parameters we take $\omega_0 = 55$ meV and $\omega_1 = 105$ meV, which produces a gap of $\sim 80 - 90$ meV between the flat bands and the higher-energy bands, depending on the strength of interactions (see Sec. 4 and also Ref. 6), similar to that observed in the experiment. The corresponding ratio $\eta = w_0/w_1 \approx 0.52$ is closer to the chiral limit[7] $\eta = 0$ than reported in recent *ab initio* studies[2,8] of MATTG.

As shown in Ref. 1, twisted trilayer graphene possesses a mirror symmetry that interchanges the top and bottom layers. Using the eigenbasis of the mirror symmetry operator

$$\mathcal{M}_z = \begin{pmatrix} 0 & 0 & \mathbb{1}_{2\times 2} \\ 0 & \mathbb{1}_{2\times 2} & 0 \\ \mathbb{1}_{2\times 2} & 0 & 0 \end{pmatrix} \tag{8}$$

acting in the layer and sublattice space spanned by $(A_1, B_1, A_2, B_2, A_3, B_3)$, the BM Hamiltonian can be block-diagonalized to an odd-parity subspace (comprising the anti-symmetric combination of layers 1 and 3) and an even-parity subspace (comprising layer 2 and the symmetric combination of layers 1 and 3). The odd sector contributes a (rotated) Dirac cone inherited from the monolayer graphene dispersion, whereas the even subspace is analogous to twisted bilayer graphene but with an "effective" tunneling strength enhanced by a factor of $\sqrt{2}$. We can therefore estimate the magic angle of MATTG from the parameters defined above, using the condition $\alpha = w_1/(v_F k_\theta) \approx 0.6$ from MATBG[4] but multiplying the tunneling parameter w_1 by $\sqrt{2}$ to account for the symmetry transformation relating MATTG to MATBG, yielding $\theta_M \sim 1.52°$. In the presence of a perpendicular displacement field D, an interlayer potential $u = -dD/\epsilon_\perp$ is generated between neighboring layers, where $d \approx 0.33$ nm is the interlayer distance and $\epsilon_\perp$ the dielectric constant of the device in the perpendicular direction. Such a term breaks the mirror symmetry decomposition and hybridizes the flat bands with the Dirac cone.

2. SIMILARITY TO TBG AND GATE-INDUCED SECTOR MIXING

A central paradigm behind the analysis of twisted trilayer graphene's electronic properties stems from the seminal work of Refs. 1,2. This framework demonstrates that the low energy theory of twisted trilayer graphene decomposes into a twisted bilayer-like sector (with a renormalized magic angle) and a Dirac cone. Such a decomposition allows a direct consideration of correlated orders proposed in TBG to TTG, as we indeed do in the sections that follow. This paradigm has been extensively verified with a body of theoretical and experimental work, including Refs. 6,9–13.

A limiting factor of this analysis is the extent of the decoupling between the TBG-like and Dirac sectors. The leading cause of mixing between sectors is the presence of a perpendicular displacement field. Such a displacement field can be an intentional effect due to the device structure (e.g., a dual-gated device) or an unintentional impact of using a single-gated device that leads to an inhomogeneous charge distribution (with different chemical potentials on each layer). In our experiment, the latter option is relevant; we thus need to evaluate the induced layer-dependent potentials.

We model the device as a series of four metallic layers vertically stacked on top of each other. Each layer corresponds to either the metallic gate (with charge density $-n$) or one of the three graphene layers (with charge density n_1, n_2, n_3 respectively). We assume that the gate is separated by an hBN dielectric of thickness $d_{\rm hBN}$ and permittivity $\epsilon_{\rm hBN}$ from the graphene layers, which are a distance d apart from each other with a dielectric $\epsilon_\perp$ in between (we clarify the choice of $\epsilon_\perp$ later). Charge conservation requires that $n_1 + n_2 + n_3 = n$. Solving the electrostatic problem[13–15] we get the following potentials V_l in each graphene layer:

$$V_1 \equiv \mu - \frac{U}{2} - \frac{U}{4} = \mu - \frac{end}{2\epsilon_\perp\epsilon_0} - \frac{end}{4\epsilon_\perp\epsilon_0} \,, \tag{9}$$

$$V_2 \equiv \mu = \frac{end_{\rm hBN}}{\epsilon_{\rm hBN}\epsilon_0} + \frac{3end}{4\epsilon_\perp\epsilon_0} \,, \tag{10}$$

$$V_3 \equiv \mu + \frac{U}{2} - \frac{U}{4} = \mu + \frac{end}{2\epsilon_\perp\epsilon_0} - \frac{end}{4\epsilon_\perp\epsilon_0} \,. \tag{11}$$

The potentials are measured with respect to the metallic gate, ϵ_0 is the vacuum permittivity, and μ is the system's chemical potential. In arriving at these expressions, we also employed that the charge distribution of the TBG-like sector in TTG is given approximately by $n_1 = n_3 = n/4$ and $n_2 = n/2$, which follows from the structure of the BM model for this system (See Ref. 1,2,13 for a detailed derivation.).

Using the similarity transformation[1,2] that brings the Hamiltonian from the layer basis to the sector basis, we get

$$\mathcal{H} = \begin{pmatrix} h^1_\tau - \mu + \frac{U}{4} & \sqrt{2}T & \frac{U}{2} \\ \sqrt{2}T^\dagger & h^2_\tau - \mu & 0 \\ -\frac{U}{2} & 0 & h^3_\tau - \mu + \frac{U}{4} \end{pmatrix} \,, \tag{12}$$

where $h^1_\tau = h^3_\tau$ and for clarity we suppressed the $\boldsymbol{k}, \boldsymbol{r}$ and θ dependence introduced in the previous section. The back gate thus induces a standard displacement-field coupling with strength $U/2$ between the two sectors, as well as an effective displacement field $U/4$ within the TBG-like sector.

We now estimate the magnitude of the induced potential difference $U = \frac{end}{\epsilon_\perp\epsilon_0}$. At full doping, $n = 4e/\Omega$ (where $\Omega = \sqrt{3}L_M^2/2$, $d = 0.33$ nm, and $L_M \approx 8.8$ nm) we get $U{\sim}360/\epsilon_\perp$ meV. The value of the effective $\epsilon_\perp$ is not known exactly and is typically taken as a fitting parameter.

Taking $\epsilon_{\perp}\sim 11$ as in Ref. 10 we get $U\sim 33$ meV for full filling or, as relevant for the IKS physics near half-filling of $\nu=-2$, $U\sim 16.5$ meV. This estimate neglects interaction effects which act to minimize the electrostatic potential and layer inhomogeneity (see Ref. 13 for further discussion) – the quoted values of U should thus be understood as an upper bound. We incorporate this layer-induced gating inhomogeneity in our analysis (see SI Fig. 6 and further discussion in Sec. 5) and confirm that the assumption of an approximate decoupling between Dirac and the TBG-like sector is valid in the present experiment.

3. HETEROSTRAIN

The TTG samples studied in this work are subject to heterostrain that acts in an opposite way between adjacent rotated layers (a type of strain arising from lattice relaxation within the moiré unit cell and instrinsic to the sample, in contrast to strain inherited e.g. from a substrate). The combination of heterostrain and rigid twist angle has profound consequences for the low-energy flat bands[16] as well as for the phase diagram in the presence of electronic interactions[17]. This can be understood by noting that the strain energy scale $\epsilon\hbar v_F/a_0$ amounts to a few meV (and is thus comparable to the bandwidth of the moiré bands) for experimentally-relevant $\epsilon\sim 0.1-0.2\%$. Therefore, from the perspective of the low-energy bands the C_{3z} symmetry is strongly broken. Heterotrain however preserves the C_{2z} symmetry of pristine TTG.

We characterize the heterostrain following Ref. 16. We define the deformation tensor $\mathcal{E}_l$ in layer l, which includes strain in addition to the uniform rotation by the twist angle $\theta_l=(-1)^l\theta/2$, as

$$\mathcal{E}_l = R^T(\varphi_l)\begin{pmatrix}-\epsilon_l & 0\\ 0 & \nu\epsilon_l\end{pmatrix}R(\varphi_l)+R(\theta_l)-\mathbb{1} \tag{13}$$

$$\approx \begin{pmatrix}\epsilon^l_{xx} & \epsilon^l_{xy}-\theta_l\\ \epsilon^l_{xy}+\theta_l & \epsilon^l_{yy}\end{pmatrix}. \tag{14}$$

Here ϵ_l is the magnitude of strain in layer l and φ_l its direction (i.e., the angle of the compressed axis with respect to the x axis). The parameter $\nu\approx 0.16$ is the Poisson ratio for monolayer graphene. The strain tensor components are denoted by ϵ^l_{ij}. We further assume that strain acts in an identical way on the top and bottom layers (but with an opposite sign on the middle layer), i.e., $\epsilon_1=\epsilon_3=-\epsilon_2\equiv\frac{\epsilon}{2}$ and $\varphi_1=\varphi_2=\varphi_3\equiv\varphi$. Deviations from this condition are expected to lead to much weaker effects on the band structure, because the top and bottom layers are not twisted relative to one another. (In contrast, the effect of heterostrain between layers 1 or 3 and layer 2 is magnified due to their small relative twist angle.) This strain configuration preserves the mirror symmetry $\mathcal{M}_z$.

In real and momentum space, vectors on the monolayer graphene scale transform (assuming zero displacement between the layers) as

$$\boldsymbol{r}_l\to\mathcal{M}_l\boldsymbol{r}_l\ ,\ \boldsymbol{k}_l\to(\mathcal{M}_l^T)^{-1}\boldsymbol{k}_l, \tag{15}$$

with $\mathcal{M}_l=1+\mathcal{E}_l$. These transformations preserve the inner product between Bravais and reciprocal lattice vectors. The mBZ can be constructed as follows. The moiré reciprocal lattice vectors are obtained from the subtraction of the deformed reciprocal lattice vectors of monolayer graphene in the different layers as

$$\boldsymbol{g}_1=\left((\mathcal{M}_1^T)^{-1}-(\mathcal{M}_2^T)^{-1}\right)(\boldsymbol{G}_1-\boldsymbol{G}_2)\,, \tag{16}$$

$$\boldsymbol{g}_2=\left((\mathcal{M}_1^T)^{-1}-(\mathcal{M}_2^T)^{-1}\right)(-\boldsymbol{G}_1)\,. \tag{17}$$

The resulting mBZ geometry is shown in Fig. 3a. Note that the center of the strained moiré BZ, $\gamma_\tau = \frac{1}{2}\left(\boldsymbol{K}_{\tau,1} + \boldsymbol{K}_{\tau,2}\right) - \frac{\boldsymbol{g}_1}{2}$, is also displaced slightly from its original location. We also define a third moiré reciprocal lattice vector, $\boldsymbol{g}_3 = -(\boldsymbol{g}_1 + \boldsymbol{g}_2)$, for future convenience. The strained moiré Bravais lattice vectors, $\boldsymbol{a}_i$ with $i = 1, 2$, can be obtained from the $\boldsymbol{g}_j$ through the defining relation $\boldsymbol{a}_i \cdot \boldsymbol{g}_j = 2\pi\delta_{ij}$. The parameters ϵ and φ characterizing the experimental geometry are obtained by reproducing the strained Bravais lattice vectors extracted from large-area topography measurements (see also Methods section). This analysis leads to $\epsilon \approx -0.12\%$ (i.e., the middle layer is compressed while the top/bottom layers expands along the φ direction) with $\varphi \approx 87°$.

In the presence of heterostrain, the BM continuum model for TTG is affected in two ways. The first effect is geometric: the strain changes the shape of the mBZ according to the transformations outlined above. The second effect, inherited from the coupling of the underlying Dirac electrons of monolayer graphene to the strain field, is the emergence of a "pseudo" vector potential

$$\boldsymbol{A}_l = \frac{\beta}{2}(\epsilon^l_{xx} - \epsilon^l_{yy}, -2\epsilon^l_{xy}), \tag{18}$$

which couples to the microscopic momentum $\boldsymbol{k}$ through minimal substituation, $\boldsymbol{k} \to \boldsymbol{k} + \tau\boldsymbol{A}$. Here $\beta \approx 3.14$ relates the change in hopping energy to the change in distance between orbitals in monolayer graphene. The different sign of the mininal substitution between the two valleys is mandated by time-reversal symmetry.

In terms of the strain angle φ_l and magnitude ϵ_l, the strain tensor components

$$\epsilon^l_{xx} = \epsilon_l(\nu \sin^2\varphi_l - \cos^2\varphi_l), \tag{19}$$

$$\epsilon^l_{yy} = \epsilon_l(\nu \cos^2\varphi_l - \sin^2\varphi_l), \tag{20}$$

$$\epsilon^l_{xy} = (1+\nu)\epsilon_l \cos\varphi_l \sin\varphi_l, \tag{21}$$

are manifestly invariant under $\varphi_l \to \varphi_l + \pi$. The pseudo-vector potential

$$\boldsymbol{A}_l = -\frac{\beta\epsilon_l}{2}(\nu+1)(\cos 2\varphi_l, \sin 2\varphi_l) \tag{22}$$

has an additional symmetry: it is invariant under $\varphi_l \to \varphi_l + \pi/2$ followed by $\epsilon_l \to -\epsilon_l$. This last transformation however changes the geometry of the mBZ, as the Poisson ratio $\nu \neq 1$. This observation allows us to determine both the magnitude and sign of ϵ in the experiment (see also the Methods section).

In the presence of heterostrain, only C_{2z}, T and the mirror $\mathcal{M}_z$ (if the displacement field $D = 0$) remain symmetries of the problem. When diagonalizing the BM model, we enforce that its eigenfunctions respect $\mathcal{C}_{2z}\mathcal{T}$ symmetry, acting as $\left(\mathcal{C}_{2z}\mathcal{T}\right) c_l(\boldsymbol{k}) \left(\mathcal{C}_{2z}\mathcal{T}\right)^{-1} = \sigma_x c_l(\boldsymbol{k})$ on the spinor $c_l(\boldsymbol{k}) = (c_{lA}(\boldsymbol{k}), c_{lB}(\boldsymbol{k}))$, with σ_x acting on the sublattice degree of freedom, as well as time-reversal $\mathcal{T}$ which connects the two valleys. The combination of time-reversal $\mathcal{T}$ and $\mathcal{C}_{2z}$ symmetries fixes the phase structure of the numerically-obtained wavefunctions.

4. HARTREE CORRECTIONS

We then consider the effects of Coulomb interactions,

$$H_C = \frac{1}{2}\int d^2\boldsymbol{r} d^2\boldsymbol{r}' \delta\rho(\boldsymbol{r}) V_C(\boldsymbol{r} - \boldsymbol{r}') \delta\rho(\boldsymbol{r}'), \tag{23}$$

with Coulomb potential $V_C(\boldsymbol{r}) = e^2/(4\pi\epsilon|\boldsymbol{r}|)$ and $\delta\rho(\boldsymbol{r}) = \sum_j \left(c_j^\dagger(\boldsymbol{r})c_j(\boldsymbol{r}) - \langle c_j^\dagger(\boldsymbol{r})c_j(\boldsymbol{r})\rangle_{\nu=0} \right)$ denotes the electronic density *measured from the charge neutrality point,* $\nu = 0$. Here j is a combined spinor index that runs over both layer index l and sublattice A/B. We treat the dielectric constant $\epsilon = \epsilon_r\epsilon_0$ as a free parameter to account phenomenologically for screening effects – effectively adjusting the (dimensionless) relative permittivity ϵ_r. Following Refs. 18–20 we consider a mean-field decoupling of H_C where we only keep the (local) Hartree correction

$$H_H = \int d^2\boldsymbol{r} V_H(\boldsymbol{r}) \sum_j c_j^\dagger(\boldsymbol{r})c_j(\boldsymbol{r}), \tag{24}$$

with the Hartree potential

$$V_H(\boldsymbol{r}) = \int d^2\boldsymbol{r}' V_C(\boldsymbol{r} - \boldsymbol{r}') \sum_j \langle c_j^\dagger(\boldsymbol{r}')c_j(\boldsymbol{r}')\rangle_H, \tag{25}$$

and the expectation value $\langle \ldots \rangle_H$ is taken relative to the charge neutrality point, $\nu = 0$.

In the momentum-space basis defined by the Bloch wavefunctions of the BM model, The Hartree contribution reads

$$\langle \boldsymbol{k} + \boldsymbol{g}, \tau, j | H_H | \boldsymbol{k} + \boldsymbol{g}', \tau', j' \rangle = \delta_{jj'}\delta_{\tau\tau'} V_C(\boldsymbol{g} - \boldsymbol{g}')\delta\rho(\boldsymbol{g} - \boldsymbol{g}') \tag{26}$$

with the Fourier-transformed Coulomb potential $V_c(\boldsymbol{g}) = e^2/(2\epsilon_r\epsilon_0|\boldsymbol{g}|)$, and

$$\delta\rho(\boldsymbol{g}) = \sum_{\tau,n,\boldsymbol{k},\boldsymbol{g}',j}{}' \left(U_{\tau n \boldsymbol{k}}^{j,\boldsymbol{g}'} \right)^* U_{\tau n \boldsymbol{k}}^{j,\boldsymbol{g}'-\boldsymbol{g}}, \tag{27}$$

where $U_{\tau n \boldsymbol{k}}^{j,\boldsymbol{g}}$ are the Bloch-wave expansion coefficients (see also Eq. (33)) in valley τ and band n. In the above expression the $\sum'$ denotes summation over occupied states for a given filling measured with respect to the CNP as explained previously. Details of the self-consistent calculation were described in Refs. 6,10,21. Here $\delta\rho(\boldsymbol{g})$is the Fourier component of the charge density (relative to $\nu = 0$), which is self-consistently determined by demanding that it leads to the same eigen-energies than those used to compute it. In practice[18–20], it is sufficient to retain only the leading-order contributions in $V_C(\boldsymbol{g})$, i.e. the six terms with smallest momentum transfer, $\pm\boldsymbol{g}_j$ with $j = 1, 2, 3$. Because C_{3z} symmetry is broken due to heterostrain, both the Coulomb potential and the self-consistently determined $\delta\rho(\boldsymbol{g})$ parameters will also be direction dependent – however time-reversal symmetry enforces that the ± contributions remain equal. Note that contributions with $\boldsymbol{g} - \boldsymbol{g}' = 0$ are omitted, because they are cancelled by the ionic background.

5. STRAINED BANDS AND NESTING INSTABILITIES TO INTER-VALLEY COHERENT STATES

Strained band structures are shown in Fig. 3 (b),(c). As explained above, we fix the strain magnitude $\epsilon = -0.12\%$ and angle $\varphi = 87°$ to best reproduce the observed moiré Bravais lattice vectors in experiment (see also Fig. 4 (a).) We first consider the top-most valence band ot the BM model, with relatively weak electronic interactions ($\epsilon_r = 30$), as shown in Fig. 3 (b) – see also Fig 4j in the main text. The flat bands are significant deformed by strain: in particular, the minimum remains in the region around the γ point, but the maxima (located near the κ, κ' points

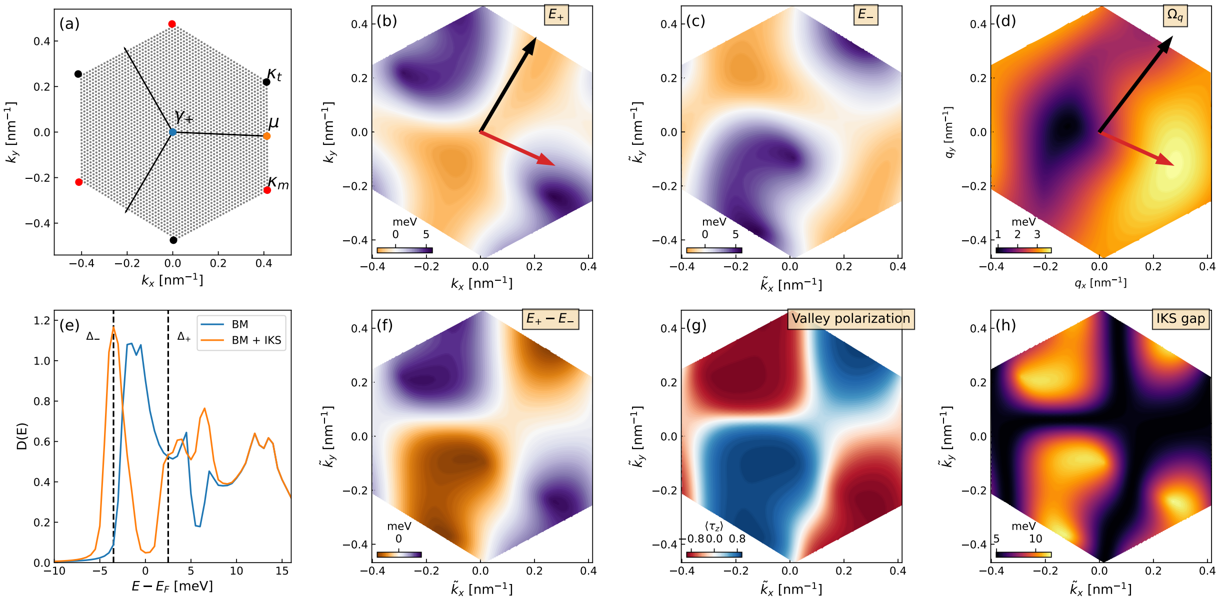

Supplementary Information Fig. 3. (a) Geometry of the strained moiré BZ, assuming strain of magnitude $\epsilon = -0.12\%$ and direction $\varphi = 87°$ and twist angle $\theta = 1.602°$. The momenta $\boldsymbol{k}$ are measured from the strained γ_+ point. Black and red circles denote Dirac points originating from the top/bottom and middle graphene layers, respectively. The three black arrows denote the direction of the strained reciprocal lattice vectors $\boldsymbol{g}_j$. The gray dots show the momentum grid used for computations, including $n_k = 3072$ points. (b): The top-most valence band of the strained BM model in valley $\boldsymbol{K}_+$, including self-consistent Hartree corrections with relative permittivity $\epsilon_r = 30$ at filling $\nu = -2$. Energies are measured from the Fermi level. We use $(w_0, w_1) = (55, 105)$ meV and $v_F \approx 8.7 \times 10^5$ m/s, which yield a first magic magic angle $\theta_m \sim 1.52°$. In the presence of strain the two Dirac cones are no longer tethered to their usual location at the corners of the moiré BZ due to the breaking of C_3 symmetry. We show the optimal IKS wavevector $\boldsymbol{q}_{\text{IKS}}$ by a red arrow, and the corresponding modulation wavevector $\boldsymbol{q}_{\text{Kekulé}}$ by a black arrow. In panel (c) we show the $\boldsymbol{K}_-$ valley (with identical parameters as in (b)), albeit shifted by $-\boldsymbol{q}_{\text{IKS}}$ – i.e., plotting in terms of the renormalized momenta $\tilde{\boldsymbol{k}} = \boldsymbol{k} + (\tau - 1)\frac{\boldsymbol{q}_{\text{IKS}}}{2}$. In the shifted coordinates the band maxima and minima of the two valleys are roughly aligned – compare panels (b) and (c). (d) The optimal IKS wavevector is selected by maximizing the function $\Omega_{\boldsymbol{q}}$ defined in Eq. 28, which computes the averaged energy separation between the valence bands in the two valleys when shifted by a relative wavevector $\boldsymbol{q}$. (f) The energy difference $E_+(\tilde{\boldsymbol{k}}) - E_-(\tilde{\boldsymbol{k}})$ between the valence bands in the two valleys, in the shifted momentum coordinates, for the optimial $\boldsymbol{q}_{\text{IKS}}$. An IKS state takes advantage of the strained band structure by developing inter-valley coherence primarily for momenta $\tilde{\boldsymbol{k}}$ where the two valleys are almost degenerate (white color in f), while keeping the other regions "locally" valley polarized (see panel g). Panel (h) shows the momentum-dependent gap opened by an IKS order with strength $\Delta_{\text{IKS}} = 2.5$ meV. (e) The density of states corresponding to panels (b) and (c) (blue line), compared with the addition of an IKS order parameter with $\Delta_{\text{IKS}} = 2.5$ meV (orange line). The IKS state opens a full gap at $\nu = -2$. The symbols $\Delta_\pm$ denote energies on either side of the IKS gap (black dashed lines) where local density of states calculations are reported in Fig. 4.

in pristine TTG) move significantly in both energy and momentum. In the presence of Coulomb interactions, Hartree corrections promote a band inversion mechanism rooted in the additional energy cost needed to host electronic states that have a strong spatial overlap[18–20,22,23]. As shown in the main text Fig. 4k for $\epsilon_r = 15$, this results in a band where the maximum now occurs near γ and the minimum occurs near one of the μ points.

The strained bands in both the weakly-interacting (non-inverted) and strongly-interacting (inverted) regimes are potentially susceptible to a type of “nesting instability” between the two valleys, where the system develops inter-valley coherence with a relative momentum shift $\boldsymbol{q}_{\mathrm{IKS}}$ that roughly aligns the maximum of one valley with the minimum of the other, as shown in Fig. 3 (b) and (c). This process allows a compromise between minimizing the exchange energy (from flavor polarization in the valley subspace) and a lower kinetic energy (from populating the lower-energy regions of the band structure in each valley[24,25]). Motivated by such an energetic picture of the IKS order, we introduce a figure of merit for the optimal IKS wavevector as

$$\Omega_{\boldsymbol{q}} = \frac{1}{N} \sum_{\boldsymbol{k}} \left| E_{+,\boldsymbol{k}} - E_{-,\boldsymbol{k}-\boldsymbol{q}} \right| . \tag{28}$$

This object computes (the absolute value of) the energy separation between the relevant bands in the two valleys $\tau = \pm$, averaged over a moiré Brillouin zone, when shifted by a relative momentum shift $\boldsymbol{q}$. (Here N is the number of moiré unit cells.) The optimal IKS wavevector $\boldsymbol{q}_{\mathrm{IKS}}$ is then obtained by maximizing $\Omega_{\boldsymbol{q}}$, as shown in Fig. 3 (d). The energy separation between bands for the optimal $\boldsymbol{q}_{\mathrm{IKS}}$ is also shown in Fig. 3 (f).

Fig. 3 (g) shows the valley polarization $\langle \tau_z \rangle$ in the IKS state constructed in such a way. The valley polarization is strongly momentum-dependent, and benefits from the ability to rotate within the Brillouin zone (in contrast to e.g. a T-IVC state). Further, developing inter-valley coherence with a finite momentum offset allows to efficiently open up a gap at $\nu = -2$, as shown in Fig. 1e and 1h. Note that the T-IVC state can also open up a gap efficiently at $\nu = 2$, by hybridizing the two Dirac points in the mini-BZ, provided that spin degeneracy is also spontaneously broken.

Comparing Fig. 4j and 4k, it is clear that interaction-induced band inversion can have a dramatic effect on the leading IKS instability – due to the discrete jump in the location of the band extrema as a function of interaction strength. In the weakly-interacting (non-inverted) regime, the preferred $\boldsymbol{q}_{\mathrm{IKS}}$ connects points in the vinicity of γ and κ, shifted and distorted by heterostrain. In contrast, in the strongly-interacting (inverted) regime, $\boldsymbol{q}_{\mathrm{IKS}}$ rather connects points in the vicinity of γ and μ. Heterostrain breaks the degeneracy between the three μ points and selects the direction of the IKS instability. In the inverted regime, strain competes against a larger (Hartree) energy scale, compared to the bare continuum model bandwidth, and is therefore less effective at distorting the band – and as a consequence, modifying the magnitude and direction of the IKS wavevector.

We study in more detail the physics of band inversion, and its influence on the IKS wavevector, as a function of the dielectric constant ϵ_r that sets the interaction energy scale. To compare more directly with experimental data, we report the Kekulé wavevector $\boldsymbol{q}_{\text{Kekulé}}$ (obtained by a constant wavevector shift from $\boldsymbol{q}_{\mathrm{IKS}}$ as described in the main text) in Fig. S5. We find that the length of $\boldsymbol{q}_{\text{Kekulé}}$ increases when the Coulomb scale is larger (smaller ϵ_r) and also when doping away from $\nu = -2$. In the non-inverted regime obtained for weaker interactions (larger ϵ_r), the magnitude of $\boldsymbol{q}_{\text{Kekulé}}$ is smaller and varies proportionally more with doping (panel **c**), more in line with experimental results. Furthermore, its direction (shown in panel **b**) is consistent with the observed experimental direction $\theta_{\text{Kekulé}} \approx 60^\circ$ – see also Fig. 4j and Fig. 4k.

To complement the discussion of Sec. 2, we analyze the robustness of $\boldsymbol{q}_{\text{Kekulé}}$ to the gate-induced displacement field in Fig. S6. We find that the magnitude of $\boldsymbol{q}_{\text{Kekulé}}$ changes by only a few percent (with respect to $U = 0$) for realistic U values of order 10 meV (Fig. S6 a–d). Similarly, the angle of $\boldsymbol{q}_{\text{Kekulé}}$ changes by only a few degrees (Fig. S6 e–h). We also observe that $\boldsymbol{q}_{\text{Kekulé}}$ is more sensitive to the layer potential U when the Coulomb interaction scale is weaker (higher ϵ_r).

Our analysis in this section neglects the role of exchange interactions – therefore, we do not determine the preferred IKS wavevector through a self-consistent solution but following a phenomenological procedure introduced in Ref.[24] and inspired by the energetics of the IKS state. Such approximations constitute limitations of our theory: specifically, a self-consistent procedure is necessary to capture both the feedback of the IKS order on the band dispersion and also to determine whether an IKS state is the relevant ground state for a given set of BM model parameters. Exclusion of the exchange (Fock) effects and displacement field D also neglects the broadening of the MATTG flat bands[20,26,27], which counteract to some extent Hartree effects[21] and thus renormalizes the parameters required for the band-inversion transition. A separate self-consistent study of the influence of all these parameters on the IKS ground state in MATTG is however called for. Nevertheless, for the purposes of identifying trends in the IKS instablities, the results of Ref.[24] for MATBG (see especially their Fig. 4) are encouraging. There the general features of the strained flat bands are only weakly affected by whether or not exchange interactions are included in the self-consistent Hartree-Fock treatment.

6. MODELING OF INTER-VALLEY COHERENT ORDERS

We now discuss in more detail symmetry-breaking orders that give rise to lattice tripling, focusing on IKS states which were found to be most consistent with the experimental data. We also briefly comment on moiré-periodic IVC states as a useful reference point.

We adopt the band basis of the (Hartree-renormalized) BM model. Such a basis is defined by operators $f_{\tau n}(\boldsymbol{k})$, which are related to the original (graphene) operators c_j used in the previous section by diagonalizing the BM model

$$f^\dagger_{\tau n}(\boldsymbol{k}) = \sum_{j\boldsymbol{g}} U^{j\boldsymbol{g}}_{\tau n \boldsymbol{k}} c^\dagger_j(\gamma_\tau + \boldsymbol{k} + \boldsymbol{g}), \tag{29}$$

In the following we focus on the active band of interest: at $\nu = -2$, the top-most valence band of the strained BM model. We drop the band index n and denote simply $f(\boldsymbol{k}) \equiv (f_+(\boldsymbol{k}), f_-(\boldsymbol{k}))^T$ the operators that annihilate electrons in valleys ± and mBZ momentum $\boldsymbol{k}$ in this band. In this basis, we can write an ansatz for a moiré-periodic IVC state as

$$H_{\text{TIVC}} = \sum_{\boldsymbol{k}} f^\dagger(\boldsymbol{k}) \Delta_{\text{IVC}}(\boldsymbol{k}) f(\boldsymbol{k}), \tag{30}$$

with $\Delta_{\text{IVC}}(\boldsymbol{k})$ an off-diagonal matrix acting in valley space, such that $\tau_x \Delta^*(-\boldsymbol{k})\tau_x = \Delta(\boldsymbol{k})$ in order to respect time-reversal symmetry. We note that this ansatz differs from the T-IVC state proposed in strong-coupling approaches, where the development of inter-valley coherence gaps out the Dirac cones near the κ and κ' points in the moiré BZ. At $\nu = -2$, for such a mechanism to be operative the spin degeneracy of the flat bands in each valley must first be lifted – either leading to a fully spin-polarized or a spin-valley-locked insulating state.

In contrast, IKS states are parametrized by a (generally incommensurate) wavevector offset $\boldsymbol{q}_{\text{IKS}}$ between the two valleys. The IKS order parameter is best described by defining a valley-dependent shifted momentum as $\tilde{\boldsymbol{k}} = \boldsymbol{k} + (\tau - 1)\boldsymbol{q}_{\text{IKS}}/2$ — in other words, $\tilde{\boldsymbol{k}}$ is a momentum label that takes value $\boldsymbol{k}$ in valley $\tau = +1$ and $\boldsymbol{k} - \boldsymbol{q}_{\text{IKS}}$ in valley $\tau = -1$. This redefinition is allowed because of a new Bloch theorem associated with an effective translation symmetry[24]. We can organize the electron operators above as $f(\tilde{\boldsymbol{k}}) \equiv (f_+(\boldsymbol{k}), f_-(\boldsymbol{k}-\boldsymbol{q}_{\mathrm{IKS}}))^T$. In this basis, one can write an ansatz for the IKS state as

$$H_{\mathrm{IKS}} = \sum_{\tilde{\boldsymbol{k}}} f^\dagger(\tilde{\boldsymbol{k}}) \Delta_{\mathrm{IKS}}(\tilde{\boldsymbol{k}}) f(\tilde{\boldsymbol{k}}). \tag{31}$$

The intuition behind this uniform shift is that it allows the maximum of one valley to lie on top of the minimum of the other valley. Then, an inter-valley type mass term can efficiently open a gap near $\nu = \pm 2$ whilst allowing the system to remain valley-polarized for momenta where that is energetically favorable – thus gaining some kinetic energy, at the expense of an exchange energy cost compared to a uniformly polarized IVC state.

For numerical simulations, we take the following ansatze for the inver-valley coherent order parameters. For the moiré-periodic IVC order we take a simple momentum-independent form $\Delta_{\mathrm{IVC}}(\boldsymbol{k}) = \Delta_{\mathrm{IVC}}\tau_x$. For the IKS state, inspired by self-consistent numerical treatments[24,25,28], we take an ansatz where the order parameter "locally" adjusts to the band structure in the shifted coordinates $\tilde{\boldsymbol{k}}$ – see Fig. 3 f. The physical intuition behind the energetics of the IKS state is that valley polarization is preferred when the difference in energy $\Delta E(\tilde{\boldsymbol{k}}) = E_+(\tilde{\boldsymbol{k}}) - E_-(\tilde{\boldsymbol{k}})$ in the two valleys is large, while inter-valley coherence is favored when the difference is small. We therefore take an ansatz

$$\Delta_{\mathrm{IKS}}(\tilde{\boldsymbol{k}}) = \Delta_{\mathrm{IKS}} \begin{pmatrix} \sin(\theta^{\mathrm{IKS}}_{\tilde{\boldsymbol{k}}}) & \cos(\theta^{\mathrm{IKS}}_{\tilde{\boldsymbol{k}}}) \\ \cos(\theta^{\mathrm{IKS}}_{\tilde{\boldsymbol{k}}}) & -\sin(\theta^{\mathrm{IKS}}_{\tilde{\boldsymbol{k}}}) \end{pmatrix}, \tag{32}$$

where $\theta^{\mathrm{IKS}}_{\tilde{\boldsymbol{k}}} = \arctan\left(\Delta E(\tilde{\boldsymbol{k}})/\gamma\right)$ parameterizes the polar angle (measured from the equator) of the valley pseudospin on the Bloch sphere. We take the IKS order parameter amplitude $\Delta_{\mathrm{IKS}} = 2.5$ meV to roughly match the energy scale of the spectroscopic (pseudo-)gap (see Extended Data Fig. 3b) and the "tilt parameter" $\gamma = 10$ meV to prepare plots in Figs. 3 and 4.

7. REAL-SPACE LDOS FEATURES

The Bloch wavefunctions corresponding to the eigenstates of the BM model read

$$\psi^j_{\tau n\boldsymbol{k}}(\boldsymbol{r}) = e^{i(\gamma_\tau + \boldsymbol{k})\cdot\boldsymbol{r}} \sum_{\boldsymbol{g}} e^{i\boldsymbol{g}\cdot\boldsymbol{r}} U^{j\boldsymbol{g}}_{\tau n\boldsymbol{k}}, \tag{33}$$

The set of vectors $\boldsymbol{g} = n_1\boldsymbol{g}_1 + n_2\boldsymbol{g}_2$ with n_1, n_2 integers are moiré reciprocal lattice vectors, truncated at finite values $-2 < n_i < 2$ in practice, and $\gamma_\tau + \boldsymbol{k}$ is the microscopic momentum associated with the electronic state labeled by the moiré mBZ momentum $\boldsymbol{k}$. The coefficients $U^{j\boldsymbol{g}}_{\tau n\boldsymbol{k}}$ are obtained from diagonalizing the BM model – including Hartree corrections, as described in Sec. 4 – and correspond to eigenvalues $E_{\tau n\boldsymbol{k}}$ labeled by the valley τ, band index n and mBZ momentum $\boldsymbol{k}$. The continuum (coarse-grained) charge density corresponding to each eigenstate can be expressed as

$$\rho_{\tau n\boldsymbol{k}}(\boldsymbol{r}) = \sum_j |\psi^j_{\tau n\boldsymbol{k}}(\boldsymbol{r})|^2 = \sum_{j\boldsymbol{g}\boldsymbol{g}'} e^{i(\boldsymbol{g}-\boldsymbol{g}')\cdot\boldsymbol{r}} U^{j\boldsymbol{g}}_{\tau n\boldsymbol{k}} \left(U^{j\boldsymbol{g}'}_{\tau n\boldsymbol{k}}\right)^*. \tag{34}$$

From this expression the local charge density at energy ω and position $\boldsymbol{r}$ can be computed using

$$\rho(\boldsymbol{r}, \omega) = -\frac{1}{\pi} \sum_{\tau n\boldsymbol{k}} \mathrm{Im}\left[\frac{\rho_{\tau n\boldsymbol{k}}(\boldsymbol{r})}{\omega + i\eta - E_{\tau n\boldsymbol{k}}}\right], \tag{35}$$

with small $\eta = 0.2$ meV to simulate thermal broadening corresponding to $T \sim 2$ K. A typical charge density profile in the moire unit cell is shown in Fig. 4a, with strain parameters relevant to the experiment and self-consistent Hartree corrections with dielectric constant $\epsilon_r = 30$.

In the presence of electronic interactions, the system may favor symmetry breaking in the spin-valley subspace. In particular, inter-valley coherent orders, which couples the two valleys, leads to eigenvalues $E_{m\boldsymbol{k}}$ associated with linear combinations of valley eigenstates of the form

$$\Psi^j_{m\boldsymbol{k}}(\boldsymbol{r}) = \sum_{\tau n} C^{\tau n}_{m\boldsymbol{k}} \psi^j_{\tau n\boldsymbol{k}}(\boldsymbol{r}) = \sum_{\boldsymbol{g}\tau n} e^{i(\gamma_\tau + \boldsymbol{g} + \boldsymbol{k})\cdot\boldsymbol{r}} C^{\tau n}_{m\boldsymbol{k}} U^{j\boldsymbol{g}}_{\tau n\boldsymbol{k}}. \tag{36}$$

The coefficients $C^{\tau n}_{m\boldsymbol{k}}$ characterizing the inter-valley coherence can be obtained, e.g., from fully self-consistent Hartree-Fock [24,25] or tensor-network[28] calculations. In this work, we adopt a more phenomenological approach and obtain the $C^{\tau n}_{m\boldsymbol{k}}$ in two steps: First, we consider self-consistent Hartree corrections to the band structure obtained from the BM model, and then we re-diagonalizing the effective Hamiltonian with inter-valley coherent mass terms, Eq. 30 or 31 depending on the type of order we wish to simulate. Motivated by modeling the STM data near $\nu = -2$, we retain only the top-most valence band of the BM model; the band index n will therefore be dropped from here on. Here we work in the basis of (Hartree-renormalized) BM bands, rather than in the Chern basis used in Ref.[29,30]. In general, the BM bands consist of a linear combination of the Chern basis eigenstates – this will have consequences later on when analyzing the LDOS patterns in real space. We also note that when considering IKS order parameters, the momentum that labels the eigenstates will be $\tilde{\boldsymbol{k}}$ instead of $\boldsymbol{k}$: see also the comment after Eq. 50.

The (continuum) charge density corresponding to a state with inter-valley coherence reads

$$\rho_{m\boldsymbol{k}}(\boldsymbol{r}) = \sum_j |\Psi^j_{m\boldsymbol{k}}(\boldsymbol{r})|^2 = \sum_{j,\boldsymbol{g},\boldsymbol{g}',\tau,\tau'} e^{i(\gamma_\tau - \gamma_{\tau'} + \boldsymbol{g} - \boldsymbol{g}')\cdot\boldsymbol{r}} C^{\tau}_{m\boldsymbol{k}} \left(C^{\tau'}_{m\boldsymbol{k}}\right)^* U^{j\boldsymbol{g}}_{\tau\boldsymbol{k}} \left(U^{j\boldsymbol{g}'}_{\tau'\boldsymbol{k}}\right)^* . \tag{37}$$

However, this quantity cannot capture Kekulé bond orders because it is a sum of local densities at each sublattice site $j = (A_1, B_1, A_2, B_2, A_3, B_3)$. Therefore, in the next section we develop a scheme, partially inspired by Ref.[29,30], to efficiently evaluate IVC order parameters on both lattice sites and bonds, in large real-space areas containing multiple moiré unit cells, comparable to those obtained in the experiment.

A. IVC order and lattice-tripling patterns

To analyze inter-valley coherent orders in real-space LDOS maps, we need to consider both on-site charge densities as well as bond orders. The on-site charge density signal arises from intra-sublattice contributions, whereas bond orders arise from inter-sublattice terms. Going beyond the continuum description (where $\boldsymbol{r}$ is a continuum variable), we need to remember that charge physically originates from the p_z atomic orbitals that are centered on discrete lattice sites $\boldsymbol{r}_j$.

We thus need to revisit the expansion in the BM model that expresses its eigenfunctions in terms of plane waves. In other words, we need to consider terms of the form

$$\langle \boldsymbol{r} | c^\dagger_{\tau j}(\gamma_\tau + \boldsymbol{k} + \boldsymbol{g}) | 0 \rangle, \tag{38}$$

where $c^\dagger_j$ above creates an electron in the low-energy expansion of monolayer graphene, with spinor index $j = (\alpha, l)$ and microscopic momentum $\gamma_\tau + \boldsymbol{k} + \boldsymbol{g}$. In the "coarse-grained" or continuum approach, one simply takes the plane-wave ansatz where

$$\langle \boldsymbol{r} | c^\dagger_j(\gamma_\tau + \boldsymbol{k} + \boldsymbol{g}) | 0 \rangle = e^{i(\gamma_\tau + \boldsymbol{k} + \boldsymbol{g})\cdot\boldsymbol{r}}, \tag{39}$$

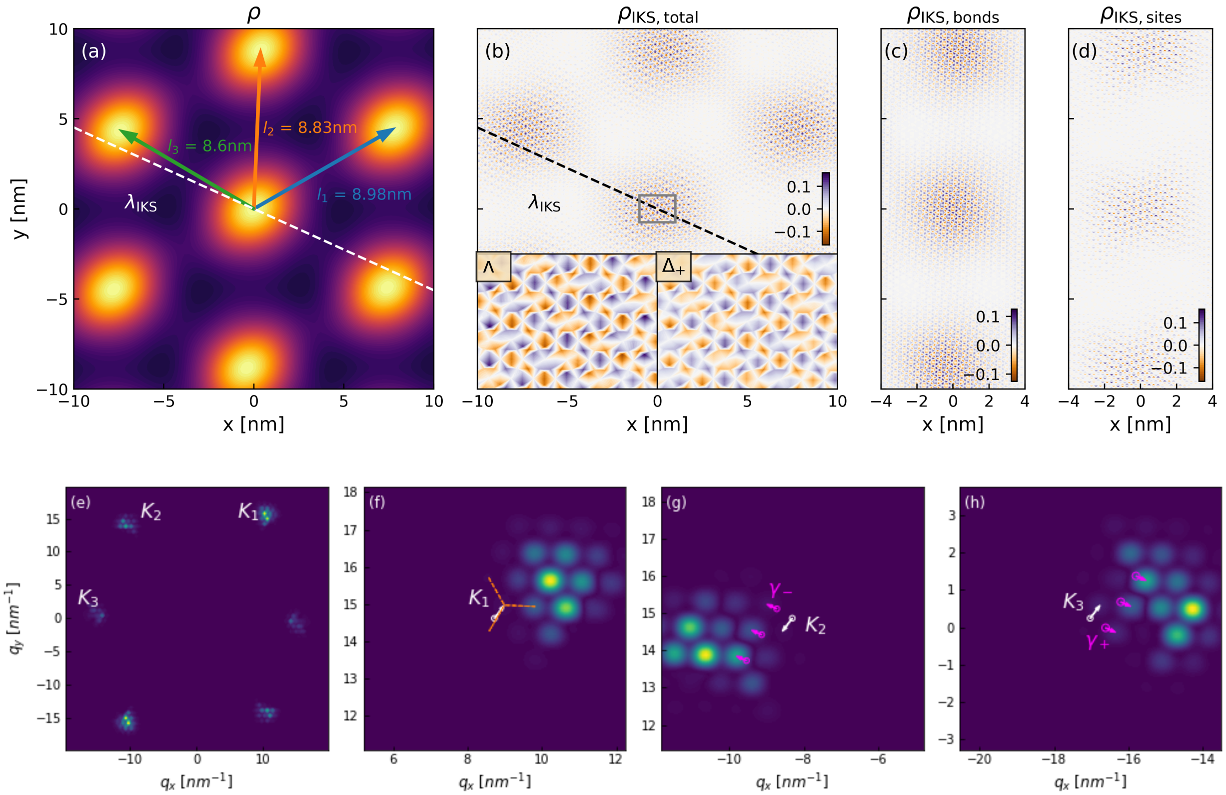

Supplementary Information Fig. 4. Signatures of IKS order in local density of states $\rho(\boldsymbol{r}, E)$, using the same parameters as for Fig. 3 (g)-(h). Panel (a) shows the continuum charge density profile computed from Eq. 34, at energy $E = \Delta_-$ (at the DOS peak below the IKS gap). The charge density is peaked at moiré AAA sites. The three Bravais lattice vectors have lengths l_1, l_2 and l_3 that match the experiment. We also note the direction of the IKS modulation by a white dashed line. Panel (b) shows the total lattice-tripling signal at $E = \Delta_-$. The two insets show a close-up of the grey box, for Δ_- as well as Δ_+ (just above the IKS gap). The contrast is inverted between the two images. Panels (c) and (d) show the site-resolved (Eq. 48) and bond-resolved (Eq. 49) channels along a stripe. Here we use "half visibility" for the bond vs site orders, $\Phi_1 = \Phi_0/2$. The incommensurability of the lattice-tripling pattern with the moire unit cell is visible by comparing neighboring AAA sites. Panels (e) to (h) show the Fourier-transformed lattice-tripling signal (from panel b) at $E = \Delta_-$. Panel (e) shows all six (first-order) lattice tripling peaks near momenta corresponding to the graphene Brillouin zone corners. A zoomed-in view of the three inequivalent regions near $\boldsymbol{K}_1$, $\boldsymbol{K}_2$, $\boldsymbol{K}_3$ is shown in panels (f) to (h). Satellite peaks separated by (strained) moiré reciprocal lattice vectors $\boldsymbol{g}$ (denoted by dashed orange lines in (f)) are resolved due to the large simulated real-space area that include multiple moiré unit cells. The peaks are however shifted from the expectation for moiré-translation invariant states (the magenta circles denote different mini-BZ centers γ_τ) by the incommensurate modulation $\boldsymbol{q}_{\rm IKS}$ (magenta arrow). Equivalently, the modulation is shifted from the graphene top-layer zone corners $\boldsymbol{K}_1$, $\boldsymbol{K}_2$ and $\boldsymbol{K}_3$ (white circles) by the momentum shift $\boldsymbol{q}_{\rm Kekulé}$ (white arrow) defined in the main text (see also Fig. 4h). The momentum shift is opposite near $\boldsymbol{K}_2$, as expected from time-reversal symmetry.

which leads to the Bloch wavefunction in Eq. 33. Incorporating the lattice, one can Fourier transform using

$$c_j^\dagger(\boldsymbol{k}) = \sum_{\boldsymbol{r}_j} e^{i\boldsymbol{k}\cdot\boldsymbol{r}_j} d^\dagger(\boldsymbol{r}_j), \tag{40}$$

where $\boldsymbol{r}_j = \boldsymbol{R}_j + \tau_j$. Here $\boldsymbol{R}_j$ is a Bravais lattice vector that labels the unit cell, and τ_j the location of the orbital on sublattice j within that unit cell. The operator $d^\dagger(\boldsymbol{r}_j)$ creates an electron in a p_z orbital at site $\boldsymbol{r}_j$, i.e.

$$\langle \boldsymbol{r}|d^\dagger(\boldsymbol{r}_j)|0\rangle = \Phi(\boldsymbol{r}-\boldsymbol{r}_j), \tag{41}$$

where the electronic wavefunction around lattice site $\boldsymbol{r}_j$ can be approximate by a Gaussian orbital,

$$\Phi(\boldsymbol{r}-\boldsymbol{r}_j) = \frac{1}{\sqrt{2\pi}\sigma} e^{-\frac{(\boldsymbol{r}-\boldsymbol{r}_j)^2}{2\sigma^2}} \tag{42}$$

with standard deviation σ. We then have

$$\langle \boldsymbol{r}|c_j^\dagger(\gamma_\tau + \boldsymbol{k} + \boldsymbol{g})|0\rangle = \sum_{\boldsymbol{r}_j} e^{i(\gamma_\tau+\boldsymbol{k}+\boldsymbol{g})\cdot\boldsymbol{r}_j} \Phi(\boldsymbol{r}-\boldsymbol{r}_j) \tag{43}$$

and thus the Bloch wavefunction associated with band m and wavevector $\boldsymbol{k}$ takes the form

$$\Psi_{m\boldsymbol{k}}(\boldsymbol{r}) = \sum_{\boldsymbol{g},\tau,j,\boldsymbol{r}_j} C^{\tau}_{m\boldsymbol{k}} U^{j\boldsymbol{g}}_{\tau\boldsymbol{k}} e^{i(\gamma_\tau+\boldsymbol{k}+\boldsymbol{g})\cdot\boldsymbol{r}_j} \Phi(\boldsymbol{r}-\boldsymbol{r}_j) \tag{44}$$

To recover the continuum description, one can take the limit $\sigma \to 0$ to make the orbitals point like, $\Phi(\boldsymbol{r}) \sim \delta(\boldsymbol{r})$, in which case Eq. 44 reduces to Eq. 36.

B. Inter-valley coherence: site vs bond order

Consider the top layer components of the wavefunction in Eq. 44 (as the STM tip primarily couples to it). The sublattice indices j now become $\alpha, \beta = A, B$. We denote by $\boldsymbol{r}_\alpha = \boldsymbol{R}_\alpha + \tau_\alpha$ the positions of all the orbitals (or graphene sites) on sublattice α. The charge density $\rho_{m\boldsymbol{k}}(\boldsymbol{r}) = |\Psi_{m\boldsymbol{k}}(\boldsymbol{r})|^2$ for each mode $m\boldsymbol{k}$ reads

$$\rho_{m\boldsymbol{k}}(\boldsymbol{r}) = \sum_{\substack{\boldsymbol{g},\boldsymbol{g}',\tau,\tau',\\ \alpha,\beta,\boldsymbol{r}_\alpha,\boldsymbol{r}_\beta}} F^{\tau\alpha\boldsymbol{g}}_{m\boldsymbol{k}} \left(F^{\tau'\beta\boldsymbol{g}'}_{m\boldsymbol{k}}\right)^* e^{i(\gamma_\tau+\boldsymbol{k}+\boldsymbol{g})\cdot\boldsymbol{r}_\alpha} e^{-i(\gamma_{\tau'}+\boldsymbol{k}+\boldsymbol{g}')\cdot\boldsymbol{r}_\beta} \Phi(\boldsymbol{r}-\boldsymbol{r}_\alpha)\Phi^*(\boldsymbol{r}-\boldsymbol{r}_\beta), \tag{45}$$

where for simplicity of notation we defined $F^{\tau\alpha\boldsymbol{g}}_{m\boldsymbol{k}} = C^{\tau}_{m\boldsymbol{k}} U^{\alpha\boldsymbol{g}}_{\tau\boldsymbol{k}}$. Computing this object for a generic grid for $\boldsymbol{r}$ is computationally intensive. However, we can simplify this expression by keeping only two types of term. First, terms with $\alpha = \beta$ correspond to on-site charge densities. In this case we keep only $\boldsymbol{r}_\alpha = \boldsymbol{r}_\beta$ contributions and neglect contributions from neighboring orbitals. The on-site contribution therefore reads

$$\rho^{\text{site}}_{m\boldsymbol{k}}(\boldsymbol{r}) = \sum_{\boldsymbol{g},\boldsymbol{g}',\tau,\tau'\alpha,\boldsymbol{r}_\alpha} F^{\tau\alpha\boldsymbol{g}}_{m\boldsymbol{k}} \left(F^{\tau'\alpha\boldsymbol{g}'}_{m\boldsymbol{k}}\right)^* e^{i(\gamma_\tau+\boldsymbol{g}-\gamma'_\tau-\boldsymbol{g}')\cdot\boldsymbol{r}_\alpha} |\Phi(\boldsymbol{r}-\boldsymbol{r}_\alpha)|^2 \tag{46}$$

We can then sample $\boldsymbol{r}$ only on the actual graphene lattice sites, replacing the continuum variable $\boldsymbol{r} \to \boldsymbol{r}_\alpha$. The intra-valley ($\tau = \tau'$) contribution reads

$$\rho^{\text{site}}_{m\boldsymbol{k}}(\boldsymbol{r}_\alpha) = |\Phi_0|^2 \sum_{\boldsymbol{g},\boldsymbol{g}',\tau} F^{\tau\alpha\boldsymbol{g}}_{m\boldsymbol{k}} \left(F^{\tau\alpha\boldsymbol{g}'}_{m\boldsymbol{k}}\right)^* e^{i(\boldsymbol{g}-\boldsymbol{g}')\cdot\boldsymbol{r}_\alpha} \tag{47}$$

where $|\Phi_0|^2$ is a number characterizing the on-site orbital visibility (which is a function of the Gaussian orbital width σ.) This expression is in essence a discretized version of the continuum charge density in Eq. 34. We can also have a site-centered signal that breaks the translation symmetry of the graphene lattice. Such a contribution comes from inter-valley ($\tau \neq \tau'$) components of Eq. 46 and reads

$$\rho^{\text{site}-\text{IVC}}_{m\boldsymbol{k}}(\boldsymbol{r}_\alpha) = |\Phi_0|^2 \sum_{\tau} e^{2i\gamma_\tau\cdot\boldsymbol{r}_\alpha} \sum_{\boldsymbol{g},\boldsymbol{g}'} F^{\tau\alpha\boldsymbol{g}}_{m\boldsymbol{k}} \left(F^{\overline{\tau}\alpha\boldsymbol{g}'}_{m\boldsymbol{k}}\right)^* e^{i(\boldsymbol{g}-\boldsymbol{g}')\cdot\boldsymbol{r}_\alpha} \tag{48}$$

with $\overline{\tau}$ denotes the opposite valley of τ, and we used that $\gamma_{\overline{\tau}} = -\gamma_\tau$.

For the lattice-tripling bond order, we consider both valley and sublattice off-diagonal contributions, $\tau \neq \tau'$ and $\alpha \neq \beta$ in Eq. 45. We want to evaluate this object on all the *nearest-neighbor bonds*, i.e. for $\boldsymbol{r} \equiv \boldsymbol{r}_{\text{AB}} = (\boldsymbol{r}_{\text{A}} + \boldsymbol{r}_{\text{B}})/2$. Let us also define $\delta\boldsymbol{r}_{\text{AB}} \equiv (\boldsymbol{r}_{\text{A}} - \boldsymbol{r}_{\text{B}})/2$, the three different vectors than connect a particular site B to its three closest bond centers. Throwing away all contributions from orbitals beyond nearest neighbors, we get

$$\begin{aligned}\rho^{\text{kekule}}_{m\boldsymbol{k}}(\boldsymbol{r}_{\text{AB}}) =& \sum_{\boldsymbol{g}\boldsymbol{g}'\tau} F^{\tau A\boldsymbol{g}}_{m\boldsymbol{k}} \left(F^{\overline{\tau}B\boldsymbol{g}'}_{m\boldsymbol{k}}\right)^* e^{i(\gamma_\tau+\boldsymbol{k}+\boldsymbol{g})\cdot(\boldsymbol{r}_{\text{AB}}+\delta\boldsymbol{r}_{\text{AB}})} e^{-i(\gamma_{\overline{\tau}}+\boldsymbol{k}+\boldsymbol{g}')\cdot(\boldsymbol{r}_{\text{AB}}-\delta\boldsymbol{r}_{\text{AB}})} \Phi(-\delta\boldsymbol{r}_{\text{AB}})\Phi^*(\delta\boldsymbol{r}_{\text{AB}}) \\ &+ (A \leftrightarrow B) \\ =& |\Phi_1|^2 \sum_{\boldsymbol{g}\boldsymbol{g}'\tau} F^{\tau A\boldsymbol{g}}_{m\boldsymbol{k}} \left(F^{\overline{\tau}B\boldsymbol{g}'}_{m\boldsymbol{k}}\right)^* e^{i(2\gamma_\tau+\boldsymbol{g}-\boldsymbol{g}')\cdot\boldsymbol{r}_{\text{AB}}} e^{i(\boldsymbol{g}+\boldsymbol{g}'+2\boldsymbol{k})\cdot\delta\boldsymbol{r}_{\text{AB}}} + (A \leftrightarrow B), \end{aligned} \tag{49}$$

where in the second line we assumed that the overlap between atomic orbitals on the three bonds, $\Phi(-\delta\boldsymbol{r}_{\text{AB}})\Phi^*(\delta\boldsymbol{r}_{\text{AB}})$, is independent of the direction of the bond and just a number $|\Phi_1|^2$.

We therefore reduced the problem to computing the local density of states on two interwoven grids: one for the sites $\boldsymbol{r}_\alpha$ and one for the bonds $\boldsymbol{r}_{\text{AB}}$. This represents a numerical speed-up by a few orders of magnitude over a brute-force approach. From these expressions we can compute the local density of states (LDOS) at energy ω and position $\boldsymbol{r}$, similarly as before, in various channels labeled by $c =$ (site, site-IVC, Kek).

$$\rho^c(\boldsymbol{r},\omega) = -\frac{1}{\pi}\sum_{m\boldsymbol{k}} \text{Im}\left[\frac{\rho^c_{m\boldsymbol{k}}(\boldsymbol{r})}{\omega + i\eta - E_{m\boldsymbol{k}}}\right]. \tag{50}$$

The expressions derived above work as stated for moiré-periodic inter-valley coherent states. However, for IKS states we must remember that the momentum label for the eigenstates is actually $\tilde{\boldsymbol{k}}$. However, the physical momentum appearing in the Fourier transforms must remain $\boldsymbol{k}$, which is related to $\tilde{\boldsymbol{k}}$ by $\boldsymbol{k} = \tilde{\boldsymbol{k}} - (\tau - 1)\frac{\boldsymbol{q}_{\text{IKS}}}{2}$. We can therefore use the above expressions (Eqs. 47, 48 and 49), but where the sum over momentum labels runs over $\tilde{\boldsymbol{k}}$, and the mBZ centers are appropriately shifted, $\gamma_\tau \to \gamma_\tau - (\tau - 1)\frac{\boldsymbol{q}_{\text{IKS}}}{2}$.

8. ANALYSIS OF LDOS PATTERNS FOR INTER-VALLEY COHERENT STATES

Using the above approach we compute the lattice-tripling LDOS signal, using both the site-resolved and bond-resolved expressions Eqs. 48 and 49. For both moiré-periodic IVC (not shown here) and IKS states (shown in Fig. 4(b)–(d)), the lattice-tripling pattern is strongest around the AAA regions of the moiré unit cell, and its contrast is reversed when comparing energies just above and below the Fermi energy – two features that are also present in the experimental data. The main difference between the two candidate orders is that in an IKS state, the symmetry-breaking pattern winds along a real-space direction set by $\boldsymbol{q}_{\text{IKS}}$. The corresponding modulation wavelength $\lambda_{\text{IKS}} = 2\pi/|\boldsymbol{q}_{\text{IKS}}|$ is generally incommensurate with the size of the moiré unit cell, such that the real-space symmetry-breaking pattern differs between neighboring AAA sites[24] (except in the direction perpendicular to $\boldsymbol{q}_{\text{IKS}}$). The relative magnitude of the bond-centered and the site-centered channels depends on the ratio Φ_1/Φ_0 which characterizes the width of the p_z orbitals: we take a ratio $\Phi_1/\Phi_0 = 1/2$ in the plots in Fig. 4, which leads to a substantial bond signal.

We stress that our analysis is based on instabilities of the (Hartree-renormalized) bands of the BM model, which consist of a linear combination of different Chern sectors. In the chiral limit the Chern sectors are defined by the relation $\mathcal{C} = \tau_z\sigma_z$, i.e. they comprise states that are valley-sublattice locked. Therefore, IVC order parameters can be conveniently decomposed into intra-Chern and inter-Chern components. The resulting density of states respectively live on the bonds – for intra-Chern components, which couple e.g. $(\boldsymbol{K}, A)$ and $(\boldsymbol{K}', B)$ – and sites – for inter-Chern components, which couple e.g. $(\boldsymbol{K}, A)$ and $(\boldsymbol{K}', A)$ – of the graphene lattice. Therefore, in our case both site-and bond-centered signals are generically expected, and indeed observed in Fig. 4.

The key difference between the LDOS of the IKS and moiré-periodic IVC states resides in the breaking of translation symmetry on the moiré scale. Such a feature can be most cleanly captured by considering the Fourier-transformed lattice-tripling LDOS signal,

$$\rho^{\text{lt}}(\boldsymbol{q}, \omega) = \sum_{\boldsymbol{r}} e^{i\boldsymbol{q}\cdot\boldsymbol{r}} W(\boldsymbol{r}) \rho^{\text{lt}}(\boldsymbol{r}, \omega), \tag{51}$$

where we defined $\rho^{\text{lt}}(\boldsymbol{r}, \omega) \equiv \rho^{\text{Kek}}(\boldsymbol{r}, \omega) + \rho^{\text{site}-\text{IVC}}(\boldsymbol{r}, \omega)$, and to reduce finite-size effects we introduced the Hanning window

$$W\left(\boldsymbol{r} = (x, y)\right) = \cos^2\left(\frac{\pi y}{2L_y}\right)\cos^2\left(\frac{\pi x}{2L_x}\right), \tag{52}$$

where $L_{x,y}$ are the lengthscales that define the field of view along the x and y directions.

The calculated Fourier-transformed lattice-tripling signals are shown in Fig. 4 (e)-(h). The lattice-tripling signal occurs, as expected, near momentum transfer $\boldsymbol{K}_1$, $\boldsymbol{K}_2$ and $\boldsymbol{K}_3$ that correspond to the corners of the Brillouin zone of monolayer graphene (panel e). A zoomed-in view near each of those momenta however reveals a much richer structure. First, a number of "satellite" peaks, translated by integers of the (strained) moiré reciprocal lattice vectors $\boldsymbol{g}$, captures the intra-unit cell structure of the inter-valley coherence order. Such peaks are however shifted from naive expectations: none of the peaks line up with the moiré BZ centers $\gamma_\pm$, denoted by magenta circles in each of the panels Fig. 4 (f)-(h), which characterize the LDOS in a moiré-periodic state such as Eq. 30. Instead, the peaks are shifted by the IKS wavevector $\boldsymbol{q}_{\text{IKS}}$. Equivalenty, the observed peaks are shifted by the momentum $\boldsymbol{q}_{\text{Kekulé}}$ from the position of the strained Dirac points $\boldsymbol{K}_1$, $\boldsymbol{K}_2$, $\boldsymbol{K}_3$ as shown by the white circles and arrows in Fig. 4 (f)-(h) (see also Fig. 4h for a schematic of the modulation wavevector extraction from FT LDOS maps).

We also observe that the IKS state breaks C_3 symmetry on the microscopic graphene scale, as evident from the different Fourier-transformed intensities near the Brillouin zone corners $\boldsymbol{K}_1$, $\boldsymbol{K}_2$ and $\boldsymbol{K}_3$, see panel (e). This rotation-symmetry breaking feature seems to be also observed in the experiment (compare to Fig. 4, panels e to g). We also observe more subtle features in the variation of intensity between satellite peaks, which seems to be cut off abruptly along one-dimensional lines (e.g. near $\boldsymbol{K}_1$, panels e and f). This feature is similar to the "sashes" identified theoretically in Ref.[29] and highlighted in Fig. 4a.

9. THEORETICAL SCENARIO FOR AN INCOMMENSURATE-COMMENSURATE TRANSITION IN THE KEKULÉ SPIRAL

In this Section, we investigate possible commensuration effects on the IKS states, motivated by the data shown in Fig. 3. We start by defining the Kekulé spiral order parameter as a real vector $\boldsymbol{I}_{\boldsymbol{q}} \equiv \left(I^x_{\boldsymbol{q}}, I^y_{\boldsymbol{q}}\right)$ with

$$I^x_{\boldsymbol{q}} = \frac{1}{N}\sum_{\boldsymbol{k}} \langle \psi^\dagger_{\boldsymbol{k},\boldsymbol{q}} \tau_x \psi_{\boldsymbol{k},\boldsymbol{q}} \rangle \ , \qquad I^y_{\boldsymbol{q}} = \frac{1}{N}\sum_{\boldsymbol{k}} \langle \psi^\dagger_{\boldsymbol{k},\boldsymbol{q}} \tau_y \psi_{\boldsymbol{k},\boldsymbol{q}} \rangle, \tag{53}$$

where $\psi_{\boldsymbol{k},\boldsymbol{q}} = (\psi^+_{\boldsymbol{k}+\frac{\boldsymbol{q}}{2}}, \psi^-_{\boldsymbol{k}-\frac{\boldsymbol{q}}{2}})^T$ denote operators for electrons in the active band of interest (e.g., the top-most valence band at $\nu = -2$) and valley index $\tau = \pm$ denoted as a superscript; N is a normalization factor counting the number of unit cells. Note that the operators in the two valleys are shifted by the IKS wavevector $\boldsymbol{q}$, similarly to Sec. 6, but with an opposite shift $\pm\boldsymbol{q}/2$ in the two valleys in order to simplify the symmetry transformations – see below. Note that our order parameter definition differs from Ref. 24.

Under the relevant symmetries of the problem—namely, (spinless) time-reversal $\mathcal{T}$, π rotations C_{2z} around an out-of-plane axis, $U(1)_V$ valley rotations and translations $T_{\boldsymbol{R}}$ by moiré lattice vectors $\boldsymbol{R}$—the fermion operators transform as

$$\mathcal{T}\psi_{\boldsymbol{k},\boldsymbol{q}}\mathcal{T}^{-1} = \mathcal{K}\tau_x\psi_{-\boldsymbol{k},\boldsymbol{q}} \ , \qquad \mathcal{C}_{2z}\psi_{\tilde{\boldsymbol{k}}}\mathcal{C}_{2z}^{-1} = \tau_x\psi_{-\boldsymbol{k},\boldsymbol{q}} \tag{54}$$

$$U(1)_V\psi_{\boldsymbol{k},\boldsymbol{q}}U(1)_V^{-1} = e^{i\phi\tau_z/2}\psi_{\boldsymbol{k},\boldsymbol{q}} \ , \qquad T_{\boldsymbol{R}}\psi_{\boldsymbol{k},\boldsymbol{q}}T_{\boldsymbol{R}}^{-1} = e^{i\left(\boldsymbol{k}+\tau_z\frac{\boldsymbol{q}}{2}\right)\cdot\boldsymbol{R}}\psi_{\boldsymbol{k},\boldsymbol{q}}. \tag{55}$$

Under the symmetries outlined above, the IKS order parameter transforms as

$$\mathcal{T}\boldsymbol{I}_q\mathcal{T}^{-1} = \boldsymbol{I}_q \ , \qquad \mathcal{C}_{2z}\boldsymbol{I}_{\boldsymbol{q}}\mathcal{C}_{2z}^{-1} = \begin{pmatrix} I^x_{\boldsymbol{q}} \\ -I^y_{\boldsymbol{q}} \end{pmatrix} \tag{56}$$

$$U(1)_V\boldsymbol{I}_{\boldsymbol{q}}U(1)_V^{-1} = R(\phi)\boldsymbol{I}_{\boldsymbol{q}} \ , \qquad T_{\boldsymbol{R}}\boldsymbol{I}_{\boldsymbol{q}}T_{\boldsymbol{R}}^{-1} = R(\boldsymbol{q}\cdot\boldsymbol{R})\boldsymbol{I}_{\boldsymbol{q}} \tag{57}$$

with $R(\phi)$ the usual two-dimensional rotation matrix. As evident from the above symmetry transformations, the IKS state is characterized by spontaneously-broken translation and $U(1)_V$ symmetries. However, the product $T'_{\boldsymbol{R}} = T_{\boldsymbol{R}}U(1)_V$ is preserved, for a judiciously chosen valley phase rotation $\phi = -\boldsymbol{q}\cdot\boldsymbol{R}$ that cancels out the contribution from translation.

We can write a Ginzburg-Landau free energy for the IKS order as

$$F^{\mathrm{IKS}}_{\boldsymbol{q}} = r_I|\boldsymbol{I}_{\boldsymbol{q}}|^2 + U_I|\boldsymbol{I}_{\boldsymbol{q}}|^4 + \cdots \tag{58}$$

where all couplings are real (and in general $\boldsymbol{q}$ dependent). Such a free energy varies smoothly with $\boldsymbol{q}$, and thus at this level lock-in to commensurate wavevectors will not arise. We should however remember that $U(1)_V$ valley rotation symmetry in TTG is only emergent at low energies. Indeed, crystal momentum conservation on the microscopic graphene scale only enforces a Z_3 symmetry. If $U(1)_V$ is broken down to Z_3, the first expression in Eq. (57) should be replaced by the weaker condition

$$Z_3 \boldsymbol{I}_{\boldsymbol{q}} Z_3^{-1} = R\left(\frac{2\pi j}{3}\right) \boldsymbol{I}_{\boldsymbol{q}} \tag{59}$$

with $j = 0, 1, 2$. As a consequence, *for particular commensurate IKS wavevectors* $\boldsymbol{q}_{\text{comm}}$, a new family of terms of the form

$$\delta_n \left[\left(I^+_{\boldsymbol{q}_{\text{comm}}}\right)^{3n} + \left(I^-_{\boldsymbol{q}_{\text{comm}}}\right)^{3n} \right] \tag{60}$$

with integers n can arise. Here we defined chiral order parameters $I^{\pm}_{\boldsymbol{q}} = I^x_{\boldsymbol{q}} \pm i I^y_{\boldsymbol{q}}$ for convenience, which transform as

$$\mathcal{T} I^{\pm}_{\boldsymbol{q}} \mathcal{T}^{-1} = I^{\mp}_{\boldsymbol{q}}\ ,\ \mathcal{C}_{2z} I^{\pm}_{\boldsymbol{q}} \mathcal{C}_{2z}^{-1} = I^{\mp}_{\boldsymbol{q}}\ ,\ U(1)_V I^{\pm}_{\boldsymbol{q}} U(1)_V^{-1} = e^{\pm i\phi} I^{\pm}_{\boldsymbol{q}}\ ,\ T_{\boldsymbol{R}} I^{\pm}_{\boldsymbol{q}} T_{\boldsymbol{R}}^{-1} = e^{\pm i\boldsymbol{q}\cdot\boldsymbol{R}} I^{\pm}_{\boldsymbol{q}}\ . \tag{61}$$

Preservation of translation symmetry for a given δ_n requires that wavevectors $\boldsymbol{q}_{\text{comm}}$ satisfy

$$3n\boldsymbol{q}_{\text{comm}} \cdot \boldsymbol{R} = 2\pi m \tag{62}$$

with integer m. Examples of such commensurate ordering wavevectors include $\boldsymbol{q}_{\text{comm}} = \boldsymbol{g}/3$ and $2\boldsymbol{g}/3$, which can take advantage of cubic contributions to the free energy ($n = 1$), and wavevectors $\boldsymbol{q}_{\text{comm}} = \boldsymbol{g}/6, \boldsymbol{g}/2$ which lead to a contribution to sextic order ($n = 2$). To understand how lock-in arises, suppose first that quadratic terms in $F^{\text{IKS}}_{\boldsymbol{q}}$ favor condensation at some incommensurate wavevector $\boldsymbol{q}_0$ that is 'nearby' to one of the preceding commensurate wavevectors. Lock-in occurs—without fine-tuning—when the free-energy gain from the Z_3-symmetric anisotropies accrued from condensing at $\boldsymbol{q}_{\text{comm}}$ overwhelms the energy cost from $F^{\text{IKS}}_{\boldsymbol{q}}$ that results from not selecting the otherwise optimal $\boldsymbol{q}_0$ wavevector.

While the above mechanism provides a proof-of-concept scenario for commensurate lock-in, estimates of the free energy parameters, including the relevant δ_n terms, are important for assessing resilience of the effect to thermal fluctuations and other experimentally relevant perturbations. We leave such an analysis for future work.

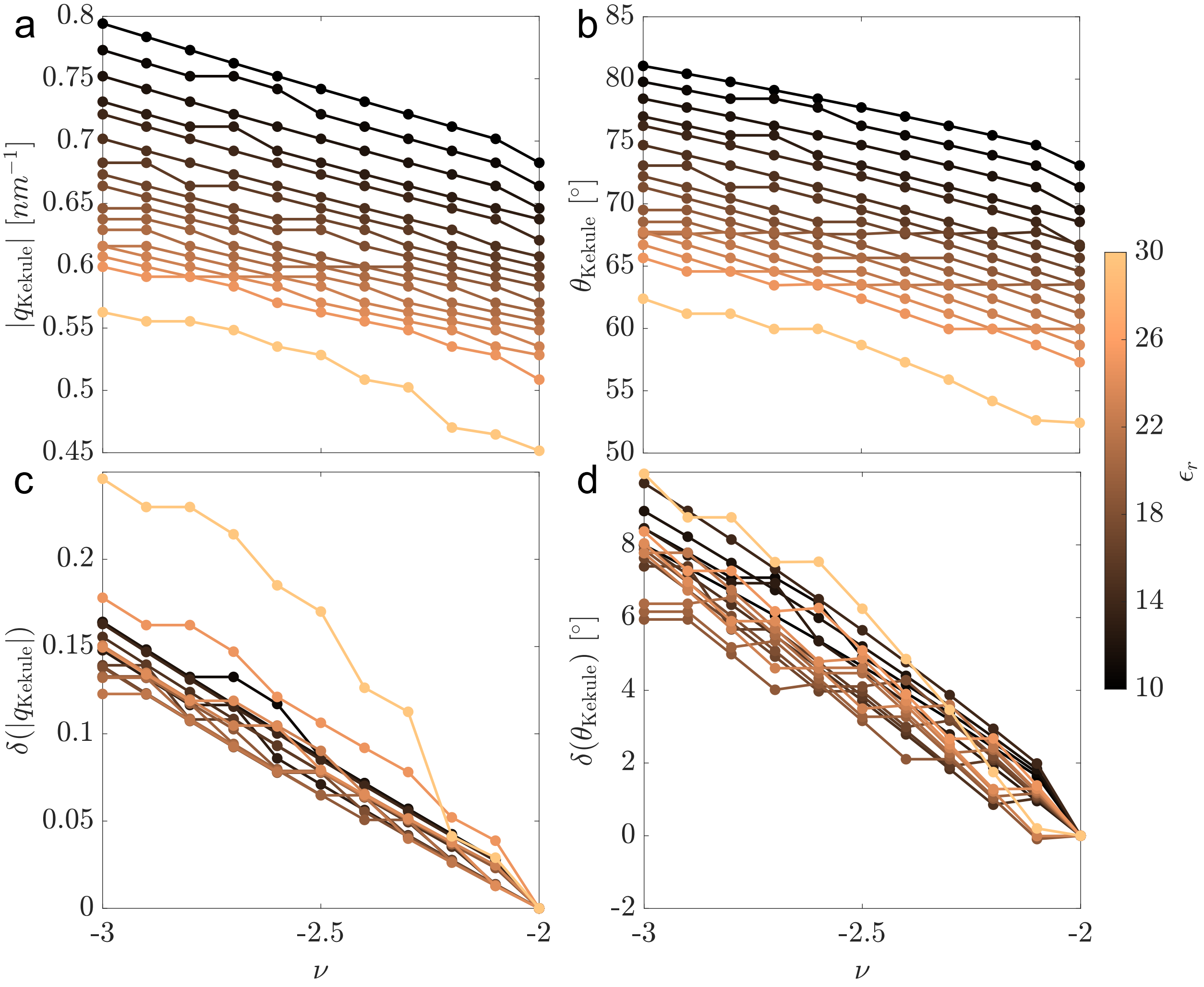

Supplementary Information Fig. 5. Hartree corrections and their consequences for IKS instabilities. All results are obtained from a self-consistent calculation of Hartree effects in MATTG, with the Kekuké wavevector $\boldsymbol{q}_{\text{Kekulé}}$ determined using the energetic picture introduced in Eq. (28). The parameters used are $\theta = 1.602°$, $w_0 = 55$ meV, $w_1 = 105$ meV, $v_F = 8.7 \times 10^5$ m/s and strain parameters $\epsilon_{\text{str}} = -0.12\%$, $\varphi = 87°$. The magnitude (panel **a**) and direction (panel **b**) of the preferred Kekulé wavevector $\boldsymbol{q}_{\text{IKS}}$ are plotted as a function of filling fraction ν between -3 and -2 for various values of ϵ_r. Panels **c** and **d** show the fractional change of these quantities with respect to the $\nu = -2$ solution for the corresponding ϵ_r.

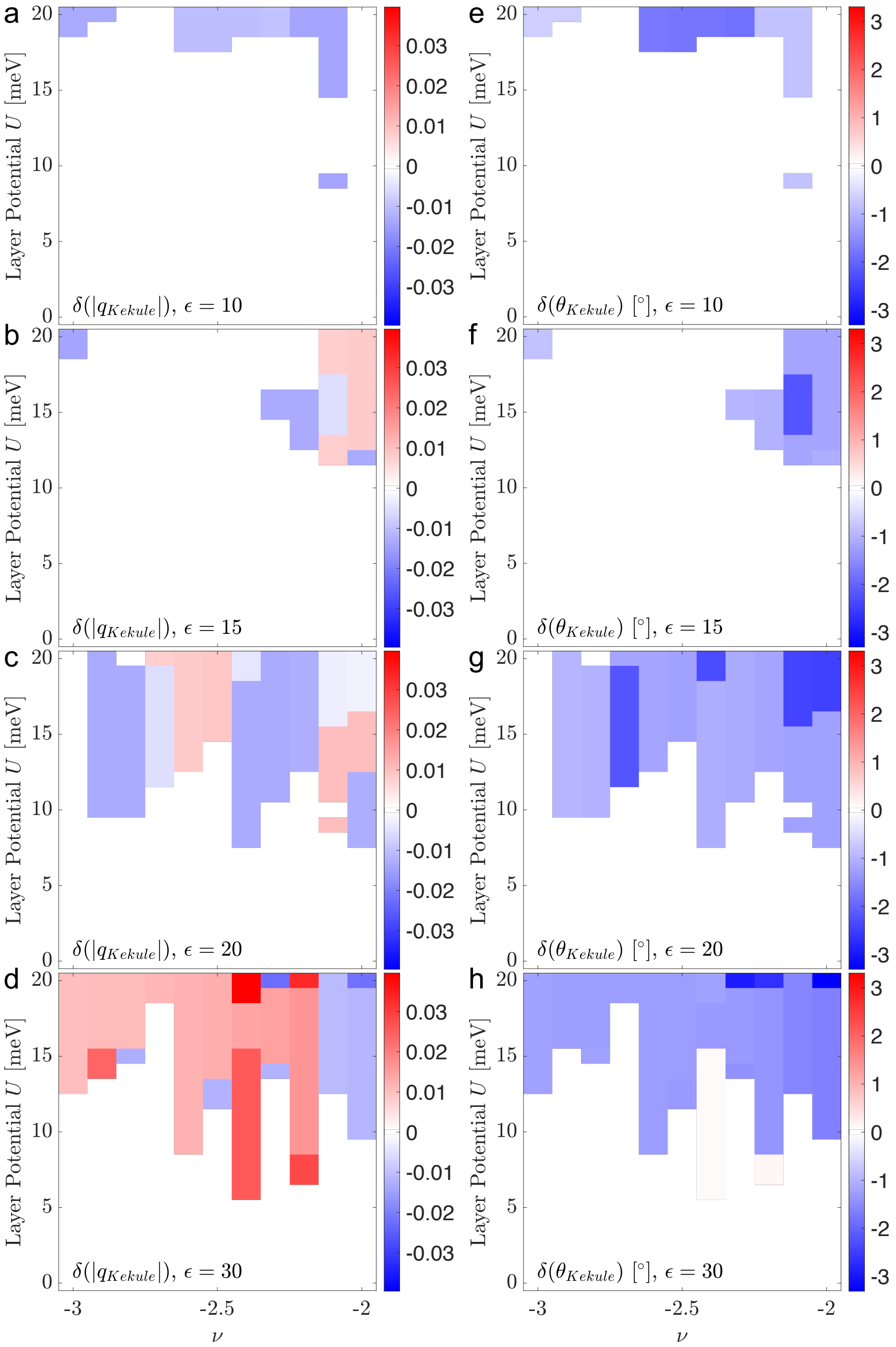

Supplementary Information Fig. 6. Fractional change in the Kekulé wavevector magnitude $|\boldsymbol{q}_{\text{Kekulé}}|$ (panels **a** through **d**), and corresponding change in its angle $\theta_{\text{Kekulé}}$ (panels **e** through **h**) as a function of layer potential U (with respect to the $U = 0$ solution). Four ϵ_r values (10, 15, 20 and 30) are used in the different rows. The parameters used are the same as in SI Fig. 5. The Kekulé wavevector is determined using the energetic picture introduced in Eq. (28). For realistic values of potential U induced by the inhomogeneous gating, which drives the hybridization between TBG-like and Dirac cone sectors (see Sec. 2), the Kekulé wavevector $\boldsymbol{q}_{\text{Kekulé}}$ is largely unchanged.

---

[1] Khalaf, E., Kruchkov, A. J., Tarnopolsky, G. & Vishwanath, A. Magic angle hierarchy in twisted graphene multilayers. *Physical Review B* **100**, 085109 (2019).

[2] Carr, S. *et al.* Ultraheavy and Ultrarelativistic Dirac Quasiparticles in Sandwiched Graphenes. *Nano Letters* **20**, 3030–3038 (2020).

[3] Lopes dos Santos, J. M. B., Peres, N. M. R. & Castro Neto, A. H. Graphene Bilayer with a Twist: Electronic Structure. *Physical Review Letters* **99**, 256802 (2007).

[4] Bistritzer, R. & MacDonald, A. H. Moiré bands in twisted double-layer graphene. *Proceedings of the National Academy of Sciences* **108**, 12233–12237 (2011).

[5] Koshino, M. *et al.* Maximally Localized Wannier Orbitals and the Extended Hubbard Model for Twisted Bilayer Graphene. *Physical Review X* **8**, 031087 (2018).

[6] Kim, H. *et al.* Evidence for unconventional superconductivity in twisted trilayer graphene. *Nature* **606**, 494–500 (2022).

[7] Tarnopolsky, G., Kruchkov, A. J. & Vishwanath, A. Origin of Magic Angles in Twisted Bilayer Graphene. *Physical Review Letters* **122**, 106405 (2019).

[8] Zhu, Z., Carr, S., Massatt, D., Luskin, M. & Kaxiras, E. Twisted Trilayer Graphene: A Precisely Tunable Platform for Correlated Electrons. *Physical Review Letters* **125**, 116404 (2020).

[9] Park, J. M., Cao, Y., Watanabe, K., Taniguchi, T. & Jarillo-Herrero, P. Tunable strongly coupled superconductivity in magic-angle twisted trilayer graphene. *Nature* **590**, 249–255 (2021).

[10] Zhang, Y. *et al.* Promotion of superconductivity in magic-angle graphene multilayers. *Science* **377**, 1538–1543 (2022).

[11] Shen, C. *et al.* Dirac spectroscopy of strongly correlated phases in twisted trilayer graphene. *Nature Materials* **22**, 316–321 (2023).

[12] Ledwith, P. J. *et al.* TB or not TB? Contrasting properties of twisted bilayer graphene and the alternating twist n-layer structures ($n = 3, 4, 5, \dots$). *arXiv:2111.11060 [cond-mat]* (2021). 2111.11060.

[13] Kolář, K., Zhang, Y., Nadj-Perge, S., von Oppen, F. & Lewandowski, C. The electrostatic fate of n-layer moiré graphene. *ArXiv* 2307.07531 (2023). 2307.07531.

[14] Koshino, M. Interlayer screening effect in graphene multilayers with ABA and ABC stacking. *Physical Review B* **81**, 125304 (2010).

[15] Guinea, F. Charge distribution and screening in layered graphene systems. *Physical Review B* **75**, 235433 (2007).

[16] Bi, Z., Yuan, N. F. Q. & Fu, L. Designing flat bands by strain. *Physical Review B* **100**, 035448 (2019).

[17] Parker, D. E., Soejima, T., Hauschild, J., Zaletel, M. P. & Bultinck, N. Strain-Induced Quantum Phase Transitions in Magic-Angle Graphene. *Physical Review Letters* **127**, 027601 (2021).

[18] Guinea, F. & Walet, N. R. Electrostatic effects, band distortions, and superconductivity in twisted graphene bilayers. *Proceedings of the National Academy of Sciences* **115**, 13174–13179 (2018).

[19] Cea, T., Walet, N. R. & Guinea, F. Electronic band structure and pinning of Fermi energy to Van Hove singularities in twisted bilayer graphene: A self-consistent approach. *Physical Review B* **100**, 205113 (2019).

[20] Cea, T. & Guinea, F. Band structure and insulating states driven by Coulomb interaction in twisted bilayer graphene. *Physical Review B* **102**, 045107 (2020).

[21] Choi, Y. *et al.* Interaction-driven band flattening and correlated phases in twisted bilayer graphene. *Nature Physics* **17**, 1375–1381 (2021).

[22] Rademaker, L., Abanin, D. A. & Mellado, P. Charge smoothening and band flattening due to Hartree

corrections in twisted bilayer graphene. *Physical Review B* **100**, 205114 (2019).

[23] Goodwin, Z. A. H., Vitale, V., Liang, X., Mostofi, A. A. & Lischner, J. Hartree theory calculations of quasiparticle properties in twisted bilayer graphene. *Electronic Structure* **2**, 034001 (2020). 2004.14784.

[24] Kwan, Y. *et al.* Kekulé spiral order at all nonzero integer fillings in twisted bilayer graphene. *Physical Review X* **11**, 041063 (2021).

[25] Wagner, G., Kwan, Y. H., Bultinck, N., Simon, S. H. & Parameswaran, S. A. Global Phase Diagram of the Normal State of Twisted Bilayer Graphene. *Physical Review Letters* **128**, 156401 (2022).

[26] Xie, M. & MacDonald, A. H. Weak-Field Hall Resistivity and Spin-Valley Flavor Symmetry Breaking in Magic-Angle Twisted Bilayer Graphene. *Physical Review Letters* **127**, 196401 (2021).

[27] Xie, M. & MacDonald, A. H. Nature of the Correlated Insulator States in Twisted Bilayer Graphene. *Physical Review Letters* **124**, 097601 (2020).

[28] Wang, T. *et al.* Kekulé spiral order in magic-angle graphene: a density matrix renormalization group study (2022). 2211.02693.

[29] Hong, J. P., Soejima, T. & Zaletel, M. P. Detecting Symmetry Breaking in Magic Angle Graphene Using Scanning Tunneling Microscopy. *Physical Review Letters* **129**, 147001 (2022).

[30] Călugăru, D. *et al.* Spectroscopy of Twisted Bilayer Graphene Correlated Insulators. *Physical Review Letters* **129**, 117602 (2022).